

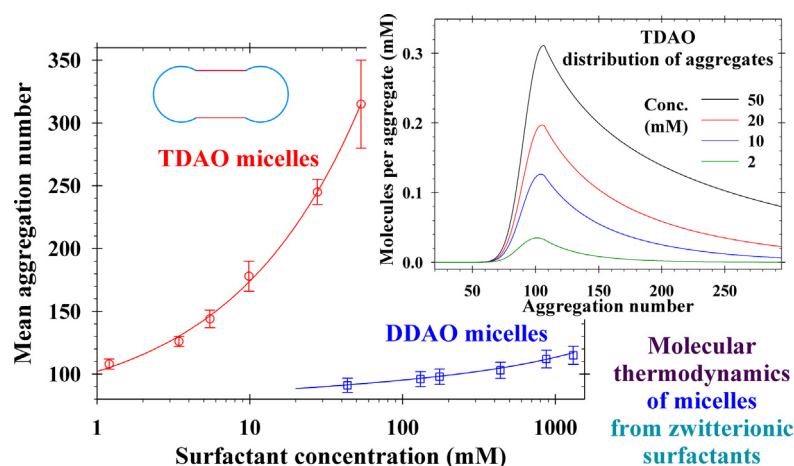


Analytical modeling of micelle growth. 5. Molecular thermodynamics of micelles from zwitterionic surfactants

Krassimir D. Danov*, Krastanka G. Marinova, Gergana M. Radulova, Mihail T. Georgiev

Department of Chemical & Pharmaceutical Engineering, Faculty of Chemistry & Pharmacy, Sofia University, 1164 Sofia, Bulgaria

GRAPHICAL ABSTRACT



ARTICLE INFO

Article history:

Received 18 May 2022

Revised 12 July 2022

Accepted 13 July 2022

Available online 16 July 2022

Keywords:

Dipole electrostatic interaction energy
Effect of micelle curvature on the free energy
Zwitterion surfactant micelles
Molecular thermodynamic theory
Size and shape of zwitterionic surfactant micelles

ABSTRACT

Hypothesis: The critical micelle concentration, aggregation number, shape and length of spherocylindrical micelles in solutions of zwitterionic surfactants can be predicted by knowing the molecular parameters and surfactant concentrations. This can be achieved by upgrading the quantitative molecular thermodynamic model with expressions for the electrostatic interaction energy between the zwitterionic dipoles and micellar hydrophobic cores of spherical and cylindrical shapes.

Theory: The correct prediction of the mean micellar aggregation numbers requires precise calculations of the free energy per molecule in the micelles. New analytical expressions for the dipole electrostatic interaction energy are derived based on the exact solutions of the electrostatic problem for a single charge close to a boundary of spherical and cylindrical dielectric media. The obtained general theory is valid for arbitrary ratios between dielectric constants, radii of spheres and cylinders, positions, and orientations of dipoles.

Findings: The detailed numerical results show quantitatively the effects of the micelle curvature and dielectric properties of the continuum media on the decrease of the dipole electrostatic interaction energy. Excellent agreement was achieved between the theoretical predictions and experimental data for the critical micelle concentration, size and aggregation number of zwitterionic surfactant micelles. This study can be extended to mixed micelles of zwitterionic and ionic surfactants in the presence of salt to interpret and predict the synergistic effect on the rheology of solutions.

© 2022 Elsevier Inc. All rights reserved.

* Corresponding author.

E-mail address: kd@lcpe.uni-sofia.bg (K.D. Danov).

1. Introduction

Many mixed surfactant solutions exhibit characteristic high viscosity peaks and variable rheological behavior depending on their concentration and particular composition, which are of primary importance for the formulation and application of such compositions in practice [1–5]. The viscosity changes are related to a significant increase in the micellar size and aggregation number. Large micellar aggregates of different sizes are typically observed in mixed surfactant solutions [6–14]. A pronounced micellar growth is measured for simple nonionic wormlike surfactant micelles from polyoxyethylene alkyl esters (experimental data are summarized in Ref. [15]) and their mixtures [9] upon concentration increase and for ionic surfactants mixed with electrolytes [14,16,17]. In contrast, the aggregation numbers of zwitterionic surfactant micelles at natural pH are relatively small [18–22], even at very high concentrations. The zwitterionic surfactants become in an ionic form with the change of pH and the growth of micellar size and the viscosity peaks have been observed in these systems as a function of pH and added electrolyte (salt) concentrations [23,24].

Prediction of the micellar growth versus the concentration and composition of surfactant solution is a problem of central importance to build a product with desirable rheological characteristics ensuring the best flow, pouring, dosing, etc. A comprehensive review on wormlike micelles and used analytical and computational theoretical approaches can be found in Refs. [15,16,25–27]. After 1990, many authors (see the literature cited in Refs. [15–17,25–29]) developed molecular thermodynamic approaches to model the critical micelle concentration (CMC), shape and size of micelles, solubilization capacity, etc., for the cases of single and mixed surfactant solutions. The precise determination of the molecular geometrical parameters and the free interaction energy per molecule are key factors in achieving a quantitative explanation of experimental data and making the molecular thermodynamic approach a predictive model. While the geometrical parameters are relatively easy to be determined precisely, the different interaction energy models could lead to distinct variations in the predictions. The total free energy per molecule in a micellar environment includes several different components, e.g. steric repulsion, conformational energy, interfacial tension component, etc.

In a series of preceding papers, detailed considerations have been presented. Quantitative models have been applied to describe precisely the interfacial tension component, f_σ [15], the steric repulsion between the headgroups of surfactant molecules, f_{hs} , by using the repulsion term in the two-dimensional van der Waals equation [15,26], the conformational free energy of the hydrocarbon chains inside the confined micellar core, f_{conf} , by the generalized Semenov model [25]. As a result, an excellent quantitative agreement between the molecular thermodynamic theory and experimental data for the scission energy, E_{sc} , for single component [15] and mixed [26] nonionic surfactants wormlike micelles have been obtained. For ionic surfactants in the presence of salt, the effects of mutual spatial confinement of the electric double layers, counterion binding, and ionic activity coefficients have been included in the description of the electrostatic component of micelle free energy, f_{ei} , to achieve a quantitative explanation of the experimental data for scission energy E_{sc} of wormlike micelles in a single ionic and mixed ionic and nonionic surfactant solutions [16,27].

When considering zwitterionic surfactant micelles, the total free energy per molecule must include the dipole component, f_{dip} , arising from the dipole–dipole repulsive interactions between zwitterionic polar headgroups, as well. Many authors used the spherical and cylindrical electrical capacitor models proposed in

Ref. [30] to calculate f_{dip} . Applying the respective expressions for f_{dip} [30], one predicts that the mean aggregation number of zwitterionic surfactant micelles (e.g. for dodecyldimethylamine oxide and betaine) considerably increases with the rise of surfactant concentration, which contradicts with the experimental observations. Note that the scission energy, E_{sc} , is equal to the number of molecules in the spherical endcaps with radius R_s multiplied by the free energy difference of the molecule in the spherical endcaps and cylindrical environment with radius R_c (Fig. 1a). An error of 0.1 $k_B T$ leads to the enormous error of 10 $k_B T$ in the scission energy for typical numbers of 100 molecules in the spherical endcaps of spherocylindrical micelles. The main assumption in the capacitor model is that the molecular dipole length, d , is much larger than the lateral distances between dipoles (surfactant headgroups) at the micelle surface. The relationship between these distances is exactly the opposite for typical geometrical micellar parameters and the capacitor model fails down (see Section 4).

The charges q and $-q$ of an individual dipole close to the boundary between micellar hydrophobic core with dielectric constant, ϵ_n , and the surrounding water phase with dielectric constant, ϵ , interact with their image charges in the nonpolar micellar core phase (Fig. 1b). As a result, a repulsive dipole free energy per zwitterionic surfactant molecule, u_d , arises. In the case of a planar dividing surface and arbitrary positions and orientations of the dipole with closest distances to the surface, s_1 and s_2 , and dipole length, d , the classical formula for the interaction energy, u_d^0 , reads [31]:

$$\frac{u_d^0}{k_B T} = (1 - 2\alpha)z_c^2 \left[\frac{L_B}{2s_1} + \frac{L_B}{2s_2} - \frac{2L_B}{(d^2 + 4s_1s_2)^{1/2}} \right] \quad (1)$$

Here: e is the elementary charge; T is the absolute temperature; k_B is the Boltzmann constant; $z_c \equiv q/e$ is the charge valence; ϵ_0 is the dielectric permittivity of vacuum; α accounts for the ratio between the dielectric constants; L_B is the Bjerrum length:

$$L_B \equiv \frac{e^2}{4\pi\epsilon_0\epsilon k_B T}, \quad \alpha \equiv \frac{\epsilon_n}{\epsilon + \epsilon_n} < 1 \quad (2)$$

Note that the interaction energy, u_d^0 , depends on the dipole parameters but it does not account in any way for the finite size or the shape of an aggregate of dipoles, i.e. the micelles. Because of the confined space of the micellar core, the repulsive interaction energy of a molecule in the micelle, u_d , depends on the micelle shape and becomes lower than u_d^0 .

The exact solution to the mathematical problem for the electrostatic potential distribution of a single charge close to an interface between two dielectric phases is reported in the literature for: spheres [32]; ellipsoids [33]; cylinders [34,35]. The respective electrostatic problems for spherical and cylindrical core–shell nanoparticles are solved in Refs. [36,37]. Using a formal analogy between electrostatics and magnetostatics, these results are also applied in the literature [38,39] for magnetically polarizable spheres and cylinders. Due to the wide practical and theoretical applications of the considered models, the general solutions to the problem of an individual charge located inside or outside dielectric spheres or cylinders are briefly presented in Section 2. Applying the superposition principle, analytical expressions for the dipole free energy are derived and illustrated numerically in Section 3 for different system parameters. The molecular thermodynamic theory upgrade for zwitterionic surfactant micelles is presented in Section 4 and the obtained results are used for a quantitative explanation of experimental data. The general conclusions are summarized in Section 5.

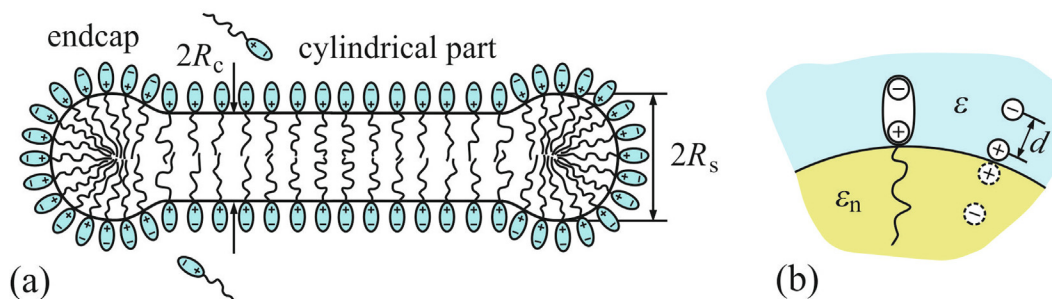


Fig. 1. (a) Sketch of spherocylindrical micelle from zwitterionic surfactants: R_s and R_c are the radii of the micellar hydrocarbon core in the regions of the endcaps and the cylindrical part. (b) Dipole surfactant head group with dipole length d , immersed in a dielectric phase with permittivity ϵ , resides close to the micellar hydrocarbon core with dielectric constant ϵ_n .

2. Electrostatic potential of a single charge in spherical and cylindrical dielectric media

Below we present the problem of an individual charge located inside or outside a dielectric sphere and a cylinder. For simplicity, the phase with dielectric constant ϵ_n is from now on referred to as the nonpolar phase and that with ϵ in which the charge is resided – as the dielectric phase or water.

In the case of a spherical dividing interface (with radius R_s and center O) between two dielectric media having dielectric constants ϵ (the aqueous phase) and ϵ_n (the nonpolar phase), one should consider two possible configurations (Fig. 2): a) a nonpolar sphere in the water (Fig. 2a); b) a nonpolar phase surrounding water. The position of the charge can be outside the sphere at distance $R_s + s$ from the center (Fig. 2a) when the nonpolar phase is inside the sphere. When the nonpolar phase is outside the sphere, the distance between the charge and center O is $R_s - s$ (Fig. 2b). The exact solutions to the electrostatic problems in spherical coordinates with radial coordinate r and polar angle θ are described in the literature [32]. Below, we summarize these solutions and apply them to calculate the respective expressions for the electrostatic interaction energies between the charge and nonpolar phase.

The distance between the charge and an arbitrary point $A(r, \theta)$ is denoted by r_A . The general solutions are presented as series with respect to the Legendre polynomials, $P_n(\cos\theta)$, where $n = 0, 1, 2, \dots$ [40], with coefficients depending on the radial coordinate, r . The detailed solutions are presented and discussed in Appendix B. For positions of charges outside the sphere (Fig. 2a), the exact solution of the considered problem for the electrostatic potential in the outer dielectric phase, φ , reads [32]:

$$\varphi = \frac{q}{4\pi\epsilon_0\epsilon R_s} \left[\frac{R_s}{r_A} + (1 - 2\alpha)S_{out}\left(\frac{s}{R_s}, \frac{r - R_s}{R_s}, \theta\right) \right] \text{ for } r \geq R_s \quad (3)$$

Here the function S_{out} accounts for the induced electrostatic potential of the nonpolar sphere. The values of S_{out} for arbitrary radial, r , and polar, θ , coordinates are calculated from the following expression (see Appendix B):

$$S_{out}\left(\frac{s}{R_s}, \frac{r - R_s}{R_s}, \theta\right) \equiv \sum_{n=1}^{\infty} \frac{n}{n + 1 - \alpha} \left(1 + \frac{s}{R_s}\right)^{-n-1} \left(1 + \frac{r - R_s}{R_s}\right)^{-n-1} P_n(\cos\theta) \quad (4)$$

In the opposite case of a charge inside the dielectric sphere, the respective exact analytical expression for the electrostatic potential in the dielectric phase, φ , is [32]:

$$\varphi = \frac{q}{4\pi\epsilon_0\epsilon R_s} \left[\frac{R_s}{r_A} + \frac{\epsilon - \epsilon_n}{\epsilon_n} + (1 - 2\alpha)S_{inn}\left(\frac{s}{R_s}, \frac{R_s - r}{R_s}, \theta\right) \right] \text{ for } r \leq R_s \quad (5)$$

where the function S_{inn} is defined as:

$$S_{inn}\left(\frac{s}{R_s}, \frac{R_s - r}{R_s}, \theta\right) \equiv \sum_{n=1}^{\infty} \frac{n + 1}{n + \alpha} \left(1 - \frac{s}{R_s}\right)^n \left(1 - \frac{R_s - r}{R_s}\right)^n P_n(\cos\theta) \quad (6)$$

Note that $S_{inn} = 0$ for $r = 0$ and hence, the induced electrostatic potential at the sphere center is not equal to zero, see the second term in the right-hand side of Eq. (5). The convergence of series in Eqs. (4) and (6) is very slow for small values of s/R_s . Simple analytical interpolations are derived and summarized in Appendix B for precise numerical calculations.

The electrostatic interaction energy, u_c , between the charge and the nonpolar phase is equal to the charge, q , multiplied by the induced electrostatic potential at the respective charge position, $r = R_s \pm s$ and $\theta = 0$, see Eqs. (3), (5), (B10) and (B23). In the case of planar dividing surfaces and arbitrary positions of the charge, the classical formula, $u_c^0 = (1 - 2\alpha)z_c^2 k_B T / (2s)$, for the interaction

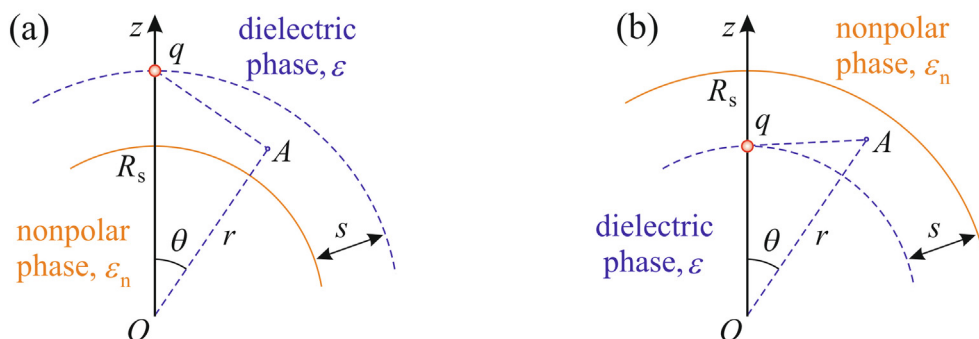


Fig. 2. Charge q is placed in water and the dividing surface between the dielectric media is a sphere with radius R_s and center O : a) the nonpolar phase is inside the sphere and the distance from the charge to the center is $R_s + s$; b) the nonpolar phase is outside the sphere and the distance from the charge to the center is $R_s - s$.

energy between the charge and nonpolar phase can be used [31]. The Bjerrum length, L_B , for water at 25 °C is 7.1 Å and even for large values of $s = 3.5$ Å and $z^2 = 1$, the scaling factor $z^2 L_B / (2s)$ in the expression for u_c^0 is equal to 1, which gives a interaction energy of about 1 $k_B T$. The difference between the interaction energies, $u_c - u_c^0$, accounts for the curvature effect of the sphere. In fact, for fixed charge positions (fixed value of s), this difference depends only on the sphere radius, R_s , and the ratio between dielectric constants, α , see Eqs. (B32) and (B38). The value of $1 - 2\alpha$ is positive for $\epsilon_n < \epsilon$ and the interaction energy is repulsive; $1 - 2\alpha$ is negative for $\epsilon_n > \epsilon$, which corresponds to attraction; at $\epsilon_n = \epsilon$, in fact, there is no boundary, according to Eq. (2) $\alpha = 0.5$ and there is no contribution from the interface as it should be.

The calculated values of the interaction energy difference, $u_c - u_c^0$, scaled with $z^2 k_B T L_B / (2s)$ for different sphere radii (s/R_s) and ratios between dielectric constants α are summarized in Fig. B2 and B4 for a charge outside the sphere and for the outer nonpolar phase, respectively. The general conclusion is that the magnitude of the interaction energy difference increases both with the decrease of sphere radii (an increase of s/R_s) and with the increase of the difference between dielectric constants (an increase of $|1 - 2\alpha|$). Because of the nonzero values of the induced electrostatic potential at the sphere center for a charge inside the sphere, see Eq. (5), the electrostatic interactions are much stronger when the dielectric constant of the outer nonpolar phase is lower than that of the inner dielectric phase (cf. Figs. B2 and B4).

In the case of cylindrical geometry, the dividing surface between the dielectric phases is a cylinder with radius R_c . In a cylindrical coordinate system $O\rho\phi z$ with axis of revolution Oz and radial and polar coordinates ρ and ϕ , the position of the charge can be outside the cylinder with charge coordinates $\rho = R_c + s$, $\phi = 0$, and $z = 0$ (Fig. 3a), when the nonpolar phase is inside the cylinder. In the opposite case (the dielectric phase is inside the cylinder), the charge coordinates are $\rho = R_c - s$, $\phi = 0$, and $z = 0$ (Fig. 3b). The exact solutions to the respective electrostatic problems [34] are described in Appendix C. The mathematical problem for a spherical dielectric media in fact is a 2D-problem because of the symmetry (Fig. 2), while in the case of a cylinder, the electrostatic problem is essentially 3D (Fig. 3). The general solution for the cylindrical geometry is presented in terms of the modified Bessel functions of the first kind, I_n , and of the second kind, K_n ($n = 0, 1, 2, \dots$) [40].

The distance between the charge and an arbitrary point $A(\rho, \phi, z)$ in the dielectric phase is denoted by r_A . For positions of charges outside the cylinder (Fig. 3a), the exact expression for the function of electrostatic potential in the outer dielectric phase, φ , reads [34]:

$$\varphi = \frac{q}{4\pi\epsilon_0\epsilon R_c} \left[\frac{R_c}{r_A} + (1 - 2\alpha)C_{out}\left(\frac{s}{R_c}, \frac{\rho - R_c}{R_c}, \phi, z\right) \right] \text{ for } \rho \geq R_c \quad (7)$$

Here the induced electrostatic potential from the inner cylindrical phase is accounted for by the function C_{out} , which for cylinders is given by the following definition:

$$C_{out}(t_1, t_2, \phi, z) \equiv \frac{2}{\pi} \int_0^\infty \frac{I_1(k)K_0[k(1+t_1)]K_0[k(1+t_2)]}{K_1(k)[1 - \alpha b_0(k)]} \cos(k \frac{z}{R_c}) dk + \frac{4}{\pi} \sum_{n=1}^\infty \int_0^\infty \frac{[I_{n+1}(k) + I_{n-1}(k)]K_n[k(1+t_1)]K_n[k(1+t_2)]}{[K_{n+1}(k) + K_{n-1}(k)][1 - \alpha b_n(k)]} \times \cos(n\phi) \cos(k \frac{z}{R_c}) dk \quad (8)$$

where $t_1 > 0$ and $t_2 \geq 0$. The dependencies of functions $b_n(k)$, defined by Eqs. (C10) and (C11), on n and k are shown in Appendix C, Fig. C1. For $n = 0, 1, 2, \dots$, the inequality $0 < b_n(k) \leq 1$ takes place and $b_n(k)$ decrease with the increase both of n and k . Therefore, the terms $1 - \alpha \leq 1 - \alpha b_n(k) < 1$ in the integrals in the right-hand side of Eq. (8) do not affect the convergence of these integrals.

For a charge inside the cylinder (Fig. 3b), the solution of the respective electrostatic problem leads to the exact result [34]:

$$\varphi = \frac{q}{4\pi\epsilon_0\epsilon R_c} \left[\frac{R_c}{r_A} + (1 - 2\alpha)C_{inn}\left(\frac{s}{R_c}, \frac{R_c - \rho}{R_c}, \phi, z\right) \right] \text{ for } \rho \leq R_c \quad (9)$$

In this case, the induced electrostatic potential from the outer cylindrical phase is accounted for by the function C_{inn} , which for cylinders is defined as follows:

$$C_{inn}(t_1, t_2, \phi, z) \equiv \frac{2}{\pi} \int_0^\infty \frac{K_0(k)I_0[k(1-t_1)]I_0[k(1-t_2)]}{I_0(k)[1 - (1-\alpha)b_0(k)]} \cos(k \frac{z}{R_c}) dk + \frac{4}{\pi} \sum_{n=1}^\infty \int_0^\infty \frac{K_n(k)I_n[k(1-t_1)]I_n[k(1-t_2)]}{I_n(k)[1 - (1-\alpha)b_n(k)]} \cos(n\phi) \cos(k \frac{z}{R_c}) dk \quad (10)$$

where $0 < t_1 < 1$ and $0 \leq t_2 \leq 1$. The terms $\alpha \leq 1 - (1 - \alpha)b_n(k) < 1$ ($n = 0, 1, 2, \dots$) in the integrands in the right-hand side of Eq. (10) again do not affect the convergence of all integrals.

The electrostatic interaction energy, u_c , between the charge and the nonpolar cylindrical phase is simply calculated by multiplying the value of the induced electrostatic potential at the charge position $\rho = R_c \pm s$, $\phi = 0$, and $z = 0$ (Fig. 3) by charge q . Hence the interaction energy difference, $u_c - u_c^0$, is given by Eqs. (C31) and (C33) in Appendix C. The numerical results for the effect of cylinder radius R_c on the electrostatic interaction energy for different ratios between the dielectric constants, α , are illustrated in Fig. C2 and C3. The final conclusions are analogous to those drawn for

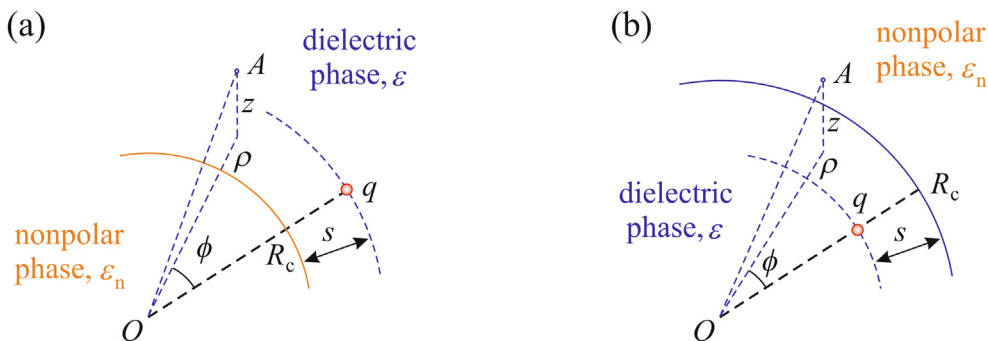


Fig. 3. Charge q placed in water phase with a dielectric constant ϵ , at a distance s to a cylindrical dividing surface with radius R_c and axis of revolution Oz : a) the nonpolar phase is inside the cylinder and the distance between the charge and the axis of revolution is $R_c + s$; b) the nonpolar phase is outside the cylinder and the distance from the charge to the axis of revolution is $R_c - s$.

spherical dielectric media. The magnitude of the interaction energy difference for cylinders at fixed distance s and $R_c = R_s$ is about two times lower than those for spheres.

3. Electrostatic interaction energy between a dipole and nonpolar phase

From the superposition principle and the general distributions of the single charge electrostatic potentials, Eqs. (3)–(10), the electrostatic interaction energy, u_d , between a dipole and a nonpolar phase can be obtained for spherical and cylindrical dielectric media. In the molecular thermodynamic approach, the part of u_d , which does not depend on the radii, is convenient to be included in the standard chemical potential of the surfactant molecule in the micellar phase, μ_m^o [15]. The difference between u_d and u_d^o , see Eq. (1), accounts for the shape and radii of the considered micelle and defines the *new* alternative form of the dipole component of the free energy per molecule, $f_{dip} = u_d - u_d^o$. The dipole component of the free energy is conveniently scaled with the corresponding value for flat interfaces through the following relationship:

$$\frac{f_{dip}}{k_B T} = z_c^2 \left[\frac{L_B}{2s_1} + \frac{L_B}{2s_2} - \frac{2L_B}{(d^2 + 4s_1s_2)^{1/2}} \right] D_{dip} \quad (11)$$

where the dimensionless function D_{dip} accounts for the curvature effects of spherical or cylindrical confined space. The reported results below are exact and valid for all possible positions and orientations of dipoles. Note that D_{dip} describes the relative change of the free energy with respect to u_d^o calculated for a planar dividing surface. The multiplier in Eq. (11) gives the magnitude of f_{dip} in $k_B T$ units. For example, in the case of dipole geometrical parameters used in Section 4 ($s_1 = 0.7$ Å and $d = 2.23$ Å), the values of the multiplier for parallel to the surface dipole orientation is 4.75 and that for perpendicular orientation is equal to 2.37.

For a *spherical dividing surface* between dielectric phases with radius R_s , the two charges of a dipole with length d have the closest distances to the spherical surface s_1 and s_2 and the polar angle, θ_d , between the radius vectors of the charge positions fulfills the relationship:

$$d^2 = (R_s \pm s_1)^2 + (R_s \pm s_2)^2 - 2(R_s \pm s_1)(R_s \pm s_2) \cos \theta_d \quad (12)$$

Here the sign plus states for dipoles outside the sphere and the minus – for dipoles inside the sphere. The coordinates of charge q are $r = R_s \pm s_1$ and $\theta = 0$ and those of charge $-q$ are $r = R_s \pm s_2$ and $\theta = \theta_d$. From the superposition principle, the induced electrostatic potential becomes a sum of those induced from both charges. The dipole electrostatic interaction energy, u_d , is a sum of the respective charges multiplied by the induced electrostatic potential in their positions (see Appendix B). The final forms of the expression for $D_{dip} = D_{out}$ in the case of a *charge outside the sphere* and for $D_{dip} = D_{inn}$ in the case of a *charge inside the sphere* read:

$$D_j = \frac{2(1 - 2\alpha)s_1s_2(d^2 + 4s_1s_2)^{1/2}}{R_s[(s_1 + s_2)(d^2 + 4s_1s_2)^{1/2} - 4s_1s_2]} \left\{ S_j \left[\frac{s_1}{R_s}, \frac{s_1}{R_s}, 0 \right] + S_j \left[\frac{s_2}{R_s}, \frac{s_2}{R_s}, 0 \right] - 2S_j \left[\frac{s_1}{R_s}, \frac{s_2}{R_s}, \theta_d \right] \right\} - (1 - 2\alpha) \text{ for } j = \text{inn, out} \quad (13)$$

Note that the induced electrostatic potential at the sphere center ($r = 0$) is equal to zero for dipoles inside the sphere, see Eq. (5), because of the electro-neutrality of the dipole. The detailed mathematical and numerical calculations are presented in Appendix B.

The numerical results for the dependence of D_{out} (a dipole outside the sphere) on the system parameters are summarized in Fig. 4. To illustrate the sphere's curvature effect, the dipole's position and orientation are fixed (s_1 , s_2 , and d are fixed) and the ratios

between dielectric constants, α , and radius R_s are varied. In the case of a perpendicular orientation of dipoles to the spherical dividing surface, the polar angle θ_d is equal to zero and $s_2 = s_1 + d$ (Fig. 4a, 4c, and 4d).

For a dipole length two times larger than the closest distance of the dipole charges to the interface ($d = 2s_1$), the dipole interaction energy, f_{dip} , increases with the decrease of the sphere radius (Fig. 4a). If the dielectric constant of the nonpolar inner phase, ϵ_n , is smaller than that of the outer phase, ϵ , then the repulsive interaction energy, u_d , decreases for the smaller sphere sizes and $f_{dip} = u_d - u_d^o < 0$. The magnitude of f_{dip} rises considerably with the decrease of R_s and for more pronounced differences between ϵ and ϵ_n . Note that the typical value of the dielectric constant for water is $\epsilon = 78$ and that for the nonpolar phase is $\epsilon_n = 2$, so that for micelles $\alpha \approx 1/40$ (see Section 4). In the opposite case $\epsilon < \epsilon_n$, the interaction energy, u_d , corresponds to an attraction and $u_d^o < 0$. The positive values of f_{dip} in Fig. 4a describe the increase of the dipole interaction energy because of the confined space of the dielectric phase in the sphere.

For a perpendicular orientation of dipoles, the increase of the dipole length, d , leads to larger charge distances s_2 and magnifies the absolute values of D_{out} for fixed ratios of dielectric constants α (Fig. 4c and 4d). The differences between the calculated curves for $d/s_1 = 1$ and $d/s_1 = 3$ seem to be small. In fact, the ratio between the scaling factors in Eqs. (11) for $d/s_1 = 3$ and that for $d/s_1 = 1$ is equal to 2.7 and the ratio between the respective dipole interaction energies, f_{dip} , becomes even >2.7 for the fixed all other system parameters. The effect of dipole orientation is illustrated in Fig. 4b for $d = 3s_1$. For a fixed dipole length, the most pronounced change in the interaction energy is observed when both dipole charges are at the closest distances to the dividing surface between the dielectric phases. This corresponds to a dipole orientation parallel to the interface and $s_2 = s_1$. The solid lines in Fig. 4b are drawn for perpendicular and the dashed lines – for parallel dipole orientations. One concludes that the dipole orientation does not affect considerably D_{out} for all ratios between the dielectric constants. The ratio between the scaling factors in Eq. (11) calculated for parallel and perpendicular dipole orientations for $d = 3s_1$ is equal to 1.98. Hence, the ratio between the respective dipole interaction energies, f_{dip} , becomes slightly smaller than 1.98. The overall conclusion is that D_{out} does not depend considerably on d/s_1 and the dipole orientation, while the magnitudes of f_{dip} are quite sensitive because of the different values of the scaling factor in Eq. (11).

For dipoles inside the dielectric sphere, the systematic study of the effects of dipole and dielectric phase parameters is illustrated in Fig. 5. From a physicochemical viewpoint, this case is realized for inverse (water in oil) microemulsions. As can be expected, the signs of D_{inn} are opposite to those of D_{out} for equal ratios between dielectric constants α (cf. Figs. 4 and 5). The magnitudes of the dipole free energy are larger than those illustrated in Fig. 4. For $\epsilon > \epsilon_n$, perpendicular dipole orientations and $d = 2s_1$ (Fig. 5a), the calculated values of D_{inn} become more than two times greater than those of D_{out} . Indeed, for a perpendicular dipole orientation, $\alpha = 1/10$, $d = 2s_1$, and $s_1/R_s = 0.25$, the calculated values are $D_{out} = -0.3283$ and $D_{inn} = 0.7491$, thus $|D_{inn}/D_{out}| = 2.828$. Note, that this result is also valid for the ratio between the respective dipole free energies. Moreover, the repulsive dipole interaction energy, u_d , considerably increases with the decrease of sphere radius R_s . This effect is less pronounced for $\epsilon < \epsilon_n$. The effect of the dipole length on D_{inn} is illustrated in Fig. 5c and 5d for $\alpha = 1/40$ and $\alpha = 9/10$, respectively. Hence, not only the magnitude and sign of D_{inn} but also the trend of the dependence on the dipole length is different than that in Fig. 4c and 4d: $|D_{inn}|$ decreases with the increase of the dipole length; the change of the dipole free energy becomes lower than those illustrated in Fig. 5c and 5d. It is interesting to

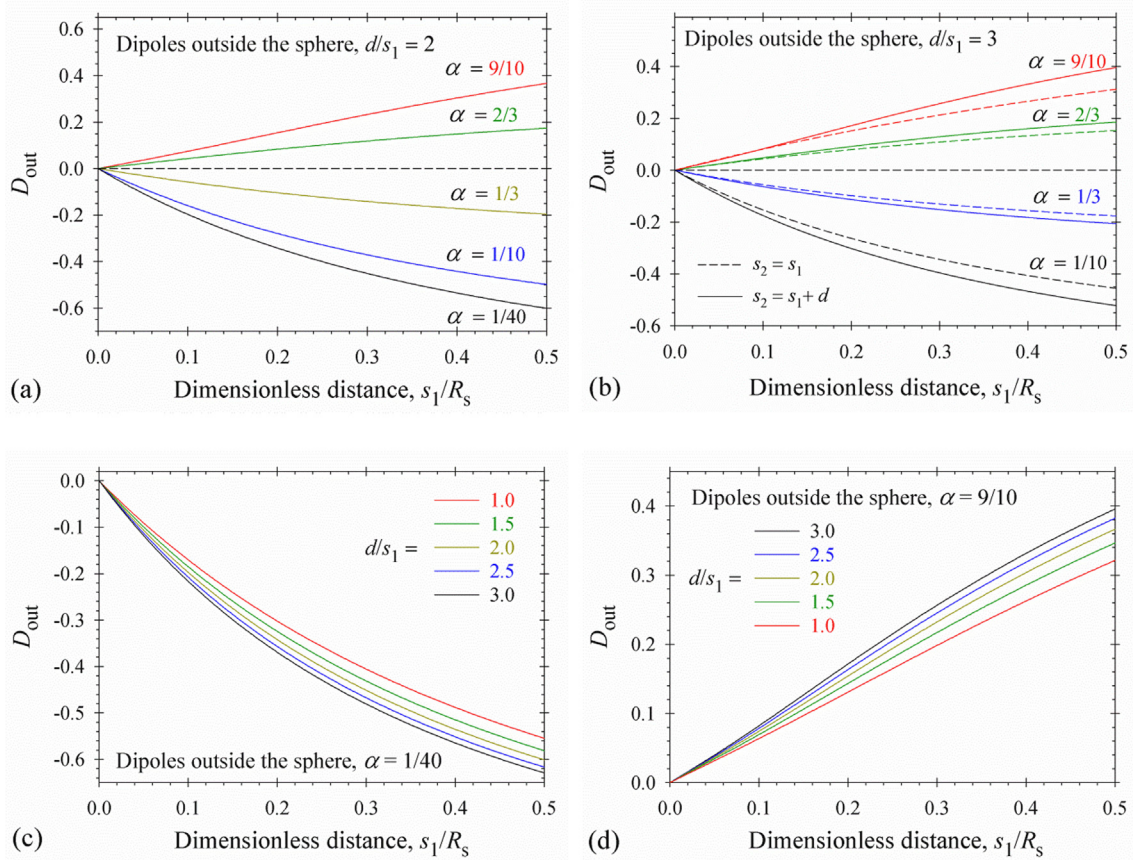


Fig. 4. Effects of the nonpolar sphere radius, R_s , and the positions and orientations of the dipole in the outer dielectric phase on the dipole interaction energy: a) $d = 2 s_1$, $s_2 = s_1 + d$, and different ratios between dielectric constants; b) $d = 3 s_1$, perpendicular ($s_2 = s_1 + d$) and parallel ($s_2 = s_1$) dipole orientations, and different values of α ; c) $\alpha = 1/40$ and d) $\alpha = 9/10$ for $s_2 = s_1 + d$, i.e. perpendicular orientation, and different values of the dipole lengths.

note that the differences between D_{inn} calculated for perpendicular (solid lines) and parallel (dashed lines) dipole orientations in the case of a dipole inside the sphere are smaller than those for D_{out} (see Fig. 5b). Thus, one can conclude that the scaling factor in Eq. (11) accounts for the main effect of the dipole orientations.

For cylindrical dielectric media, the positions of the two charges of the dipole in cylindrical coordinates are: $\rho = R_c \pm s_1$, $\phi = 0$, $z = 0$, and $\rho = R_c \pm s_2$, $\phi = \phi_d$, $z = z_d$, where the sign plus states for dipoles outside the cylinder and the minus – for dipoles inside the cylinder. The dipole length, d , can be calculated using the following relationship:

$$d^2 = (R_c \pm s_1)^2 + (R_c \pm s_2)^2 - 2(R_c \pm s_1)(R_c \pm s_2) \cos \phi_d + z_d^2 \quad (14)$$

The dipole electrostatic interaction energy, u_d , is a sum of the dipole charges multiplied by the induced electrostatic potential in their positions because of the partially confined dielectric space in the cylinder (see Appendix C). The dipole free energy is given by Eq. (11), in which the concrete form of the D_{dip} is substituted. The respective expressions for $D_{dip} = D_{out}$ in the case of a charge outside the cylinder and for $D_{dip} = D_{inn}$ for a charge inside the cylinder are:

$$D_j = \frac{2(1 - 2\alpha)s_1s_2(d^2 + 4s_1s_2)^{1/2}}{R_c[(s_1 + s_2)(d^2 + 4s_1s_2)^{1/2} - 4s_1s_2]} [C_j(\frac{s_1}{R_c}, \frac{s_1}{R_c}, 0, 0) + C_j(\frac{s_2}{R_c}, \frac{s_2}{R_c}, 0, 0) - 2C_j(\frac{s_1}{R_c}, \frac{s_2}{R_c}, \phi_d, z_d)] - (1 - 2\alpha) \text{ for } j = \text{inn, out} \quad (15)$$

The detailed mathematical and numerical calculations are presented in Appendix C.

For a dipole outside the cylindrical dielectric phase, the dependence of the interaction energy on the system parameters is illustrated in Fig. 6. The position and orientation of the dipole are fixed and the ratios between dielectric constants, α , and the radius R_c are varied. For a perpendicular orientation of dipoles to the cylindrical dividing surface, the cylindrical coordinates, ϕ_d and z_d , are equal to zero and $s_2 = s_1 + d$ (Fig. 6a, 6c, and 6d). As can be expected, the general trends are quite similar to those shown in Fig. 4 for spherical dielectric media: the increase of the dipole length and the decrease of the radius of the cylinder, R_c , lead to greater values of the dipole free energy, f_{dip} . The differences are in the magnitudes of D_{out} , c.f. Figs. 4 and 6. For example, $|D_{out}|$ for spheres is from 1.7 to 2.2 times larger than that for cylinder for the calculated examples. The effect of the dipole orientation for $\phi_d \neq 0$ and $z_d = 0$ is demonstrated in Fig. 6b. Note that the change of D_{out} is more pronounced for $\epsilon_n < \epsilon$ compared to the case $\epsilon_n > \epsilon$.

The numerical results for D_{inn} in the case of dipoles inside the cylindrical dielectric phase are summarized in Fig. 7. For a perpendicular dipole orientation, the increase both the dipole length and the radius of the cylinder, R_c , decreases $|D_{inn}|$, see Fig. 7a, 7c, and 7d. The relative differences in the magnitudes of D_{inn} between spheres and cylinders when comparing equal R_c and R_s are between 1.8 and 2.3, c.f. Figs. 5 and 7. In this case, the dipole orientations (Fig. 7b) change $|D_{inn}|$ insignificantly for all ratios between dielectric constants, α .

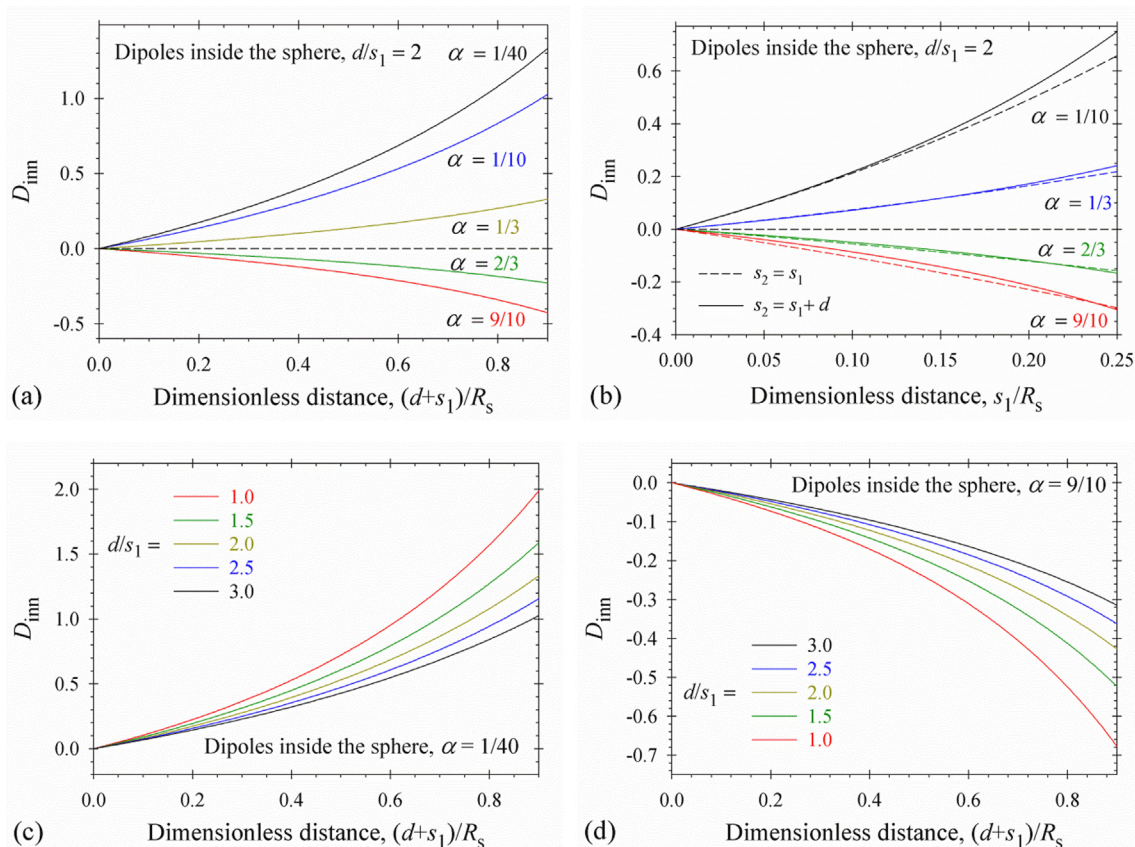


Fig. 5. Effects of the sphere radius, R_s , and the distance and orientations of the dipole inside the sphere on the dipole interaction energy: a) $d = 2 s_1$, $s_2 = s_1 + d$, and different ratios between dielectric constants; b) $d = 2 s_1$, perpendicular and parallel dipole orientations, and different values of α ; c) $\alpha = 1/40$ and d) $\alpha = 9/10$ for $s_2 = s_1 + d$, i.e. perpendicular orientation, and different values of the dipole lengths.

4. Molecular thermodynamics of zwitterionic surfactant micelles: Theory vs Experiment

Cocoamidopropyl betaine (CAPB) is more common in industrial applications [12,14,20]. From a theoretical viewpoint, there are two problems in the molecular thermodynamic theory to model the CAPB micelles. First, the samples of CAPB typically contain not negligible amount of NaCl, which should be taken into account in calculation of the free energy. Second, CAPB is a mixture of molecules with different hydrophobic chain lengths (from C10 to C16), which makes the calculation of the conformational component of the free energy difficult [25]. For that reason, the molecular thermodynamic theory of zwitterionic surfactant micelles is applied below for a quantitative explanation of the available experimental data for the CMC and aggregation numbers of zwitterionic micelles from dodecyltrimethylamine oxide (DDAO) and tetracyclodimethylamine oxide (TDAO) solutions. The contributions of the interfacial tension, f_σ , steric repulsion, f_{hs} , and conformational free energy, f_{conf} , to the total free energy of a surfactant molecule in the micellar environment are calculated using suitable physicochemical parameters and theoretical expressions as described in Appendix D. For the dipole component of the free energy, f_{dip} , we used the model presented in Sections 2 and 3.

The geometrical parameters of molecules can be retrieved from previous studies, e.g. Refs. [20,41,42]. Note that the data suggest that the DDAO and TDAO zwitterionic dipoles have a preferential parallel orientation with respect to the micellar hydrocarbon core surface. The closest dipole charge distance to the micelle hydrocarbon core depends on the nature of polar head. In the case of DDAO (TDAO) and CAPB, s_1 is the distance between N^+ and the boundary

of the micellar core and s_1 is the same for these surfactants: $s_1 = 0.7 \text{ \AA}$ [20]. The molecular thermodynamics simulations showed that the dipole moment of the surfactant headgroups in apolar solutions is equal to 5.04 Debye [41], while the effective dipole moment of the hydrated surfactant headgroup is substantially higher and equal to 10.7 Debye [42]. The dipole length calculated from the value of 10.7 Debye becomes $d = 2.23 \text{ \AA}$, so that $d = 3.18 s_1$. The dielectric constants, ϵ_n , of dodecane and tetrade-cane at room temperature are 2.01 and 2.04, respectively [43]. Processing the experimental surface tension isotherm of DDAO solutions using the van der Waals model, we obtain 35 \AA^2 for the surface area excluded by the surfactant headgroup, a_0 (see Fig. D2 in Appendix D). Hence, the minimal possible lateral distance between dipoles at the micelle surface is 6.68 \AA , which is 3 times larger than the dipole length and the main assumption in the capacitor model fails down.

For long spherocylindrical micelles (Fig. 1), the micelle scission energy, E_{sc} , is defined as: $E_{sc} = n_s(f_s - f_c)$, where n_s is the total number of molecules in the spherical endcaps, f_c and f_s are the free energies per zwitterionic molecule in the cylindrical part and spherical endcaps of micelles, respectively. The standard chemical potential is independent of micelle shape and the free energies can be replaced by the differences $\Delta f_c = f_c - \mu_m^0$ and $\Delta f_s = f_s - \mu_m^0$. The necessary parameters for the calculation of all contributions, f_σ , f_{hs} , f_{conf} , and f_{dip} , to the free energy differences and the scission energy are available and there is no need of adjustable parameters. For example, Fig. 8a shows the dependence of free energy components and Δf_c on the radius of the micelle cylindrical part, R_c , for DDAO micelles. The increase of radius R_c leads to the decrease of f_σ , and to the increase of f_{hs} , f_{conf} , and f_{dip} , as well (see Section 3 and Ref.

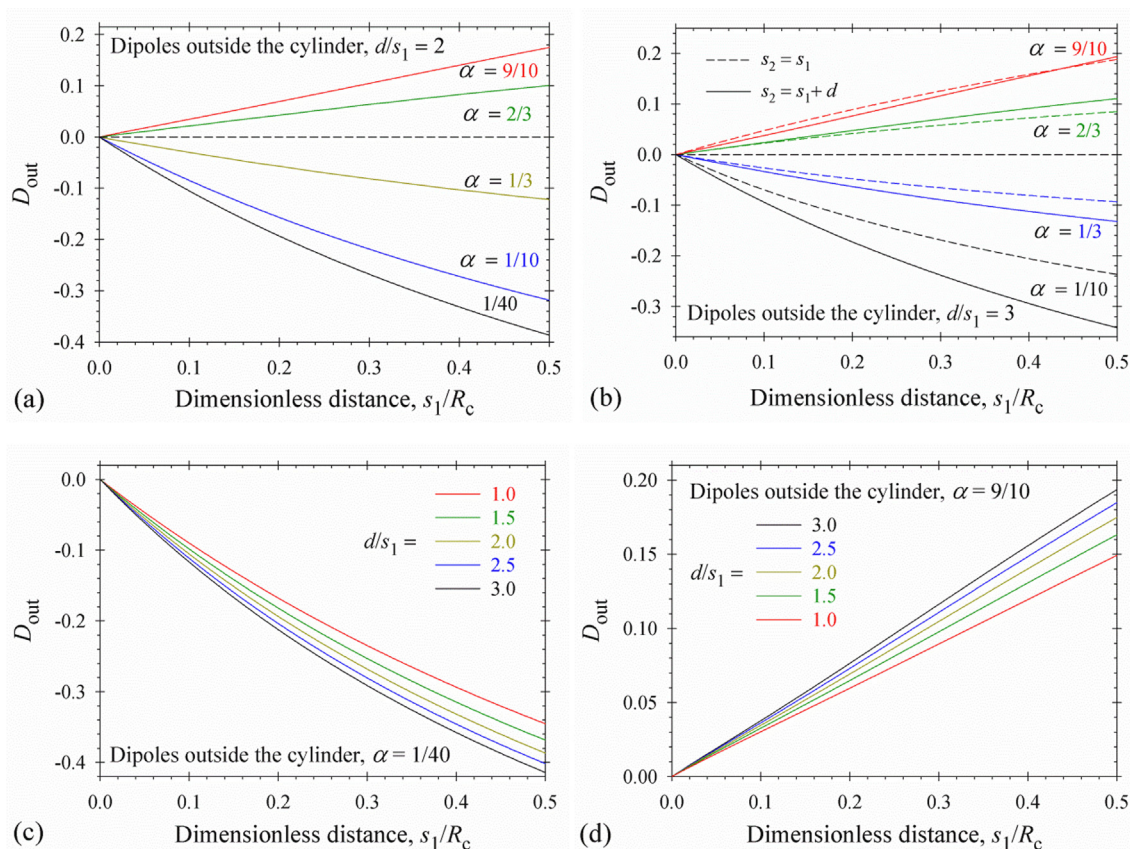


Fig. 6. Dipole interaction energy for a dipole outside a cylindrical nonpolar phase – effects of the cylindrical radius, R_c , and the dipole positions and orientations on the interaction energy: a) $d = 2s_1$, $s_2 = s_1 + d$, and different ratios between dielectric constants; b) $d = 2s_1$, perpendicular and parallel dipole orientations, and different values of α ; c) $\alpha = 1/40$ and d) $\alpha = 9/10$ for $s_2 = s_1 + d$, i.e. perpendicular orientation, and different values of the dipole lengths.

[15]). The minimum of $\Delta f_c = 4.19 k_B T$ is achieved for the optimal radius of the cylindrical part $R_c = 13.60 \text{ \AA}$. As expected, the optimal radius is lower than the extended chain length, $l = 16.7 \text{ \AA}$, of the DDAO hydrocarbon chain.

The excess free energy of the micelle spherical endcaps, E_{sc} , also represents a sum of four contributions, $E_{sc} = (E_{sc})_{\sigma} + (E_{sc})_{hs} + (E_{sc})_{conf} + (E_{sc})_{dip}$, where the subscripts refer to the respective components of the micelle free energy. The total aggregation number of the spherical endcaps, n_s , increases with the cube of radius R_s . The non-shielded area of hydrocarbon/water contact decreases with the decrease of surface curvature and as a result $(E_{sc})_{\sigma}$ decreases with the rise of R_s (Fig. 8b). In contrast, both $(E_{sc})_{hs}$ and $(E_{sc})_{conf}$ are increasing functions of R_s . Note that $|f_{dip}|$ decreases with the rise of the radii of the cylindrical part and the spherical endcaps of micelles (see Section 3). Nevertheless, $|(E_{sc})_{dip}|$ increases with the rise of R_s , because of the faster increase of n_s (Fig. 8b). The minimum of the scission energy, E_{sc} , is a fine balance of components with comparable or greater ranges of variations. The numerical results for Δf_c vs R_c and scission energy components vs R_s in the case of TDAO micellar solutions are summarized in Figs. D3a and D3b in Appendix D. Fig. D3a shows the dependence of the free energy components and Δf_c on the radius of the micelle cylindrical part, R_c , for TDAO micelles. The increase of the radius R_c leads to the decrease of f_{σ} , and the increase of f_{hs} , f_{conf} , and f_{dip} . The minimum of $\Delta f_c = 4.45 k_B T$ is achieved for the optimal radius of the cylindrical part $R_c = 15.33 \text{ \AA}$. The dependence of the excess free energy components for TDAO micelles on the radius of the spherical endcaps is shown in Fig. D3b. The respective trends for $(E_{sc})_{\sigma}$, $(E_{sc})_{hs}$, $(E_{sc})_{conf}$, and $(E_{sc})_{dip}$ are quite similar to those for DDAO illustrated in Fig. 8b.

The requirement for the local minimum of the scission energy, E_{sc} , as a function of radius R_s for a fixed optimal radius of the cylindrical part is equivalent to the chemical equilibrium between the surfactant molecules in the spherical endcaps and in the micelle cylindrical part [15]. Fig. 8c shows the dependence of E_{sc} on R_s – the minimum value of E_{sc} for DDAO micelles is equal to $10.04 k_B T$, which is achieved at the optimal radius $R_s = 16.23 \text{ \AA}$, while for TDAO micelles, the minimum of E_{sc} is equal to $16.15 k_B T$ at optimal radius $R_s = 17.93 \text{ \AA}$. In both cases, the values of the optimal radii are smaller than the respective extended chain lengths, 16.7 \AA for DDAO and 19.2 \AA for TDAO. Hence, the condition for the chemical equilibrium between the surfactant molecules in the cylindrical part and the endcaps of micellar aggregates is fulfilled. The calculated minimum of the scission energy $16.15 k_B T$ for TDAO spherocylindrical micelles is considerably larger than that for DDAO, as can be expected because of the longer chain length.

The mean mass aggregation number of rodlike micelles, n_M , can be estimated from the following formula, $n_M \approx 2(X_S - X_S^0)^{1/2} \exp[E_{sc}/(2k_B T)]$, where the molar fraction of surfactants is X_S and its value at the CMC is X_S^0 [44]. Even for concentration as high as 1 M DDAO, the estimated mean mass aggregation number of micelles using the obtained theoretical value of $E_{sc} = 10.04 k_B T$ is equal to 41, which is smaller than the aggregation number of spherical micelles 56 calculated for $R_s = l$. Hence, the scission energy of $10 k_B T$ is not enough to produce a considerable increase of the micellar aggregation number and the simple estimation of n_M cannot be used to predict the dependence of micelle aggregation number on the DDAO concentration. In contrast for 100 mM TDAO and $E_{sc} = 16.15 k_B T$, the respective value of n_M is 273, which

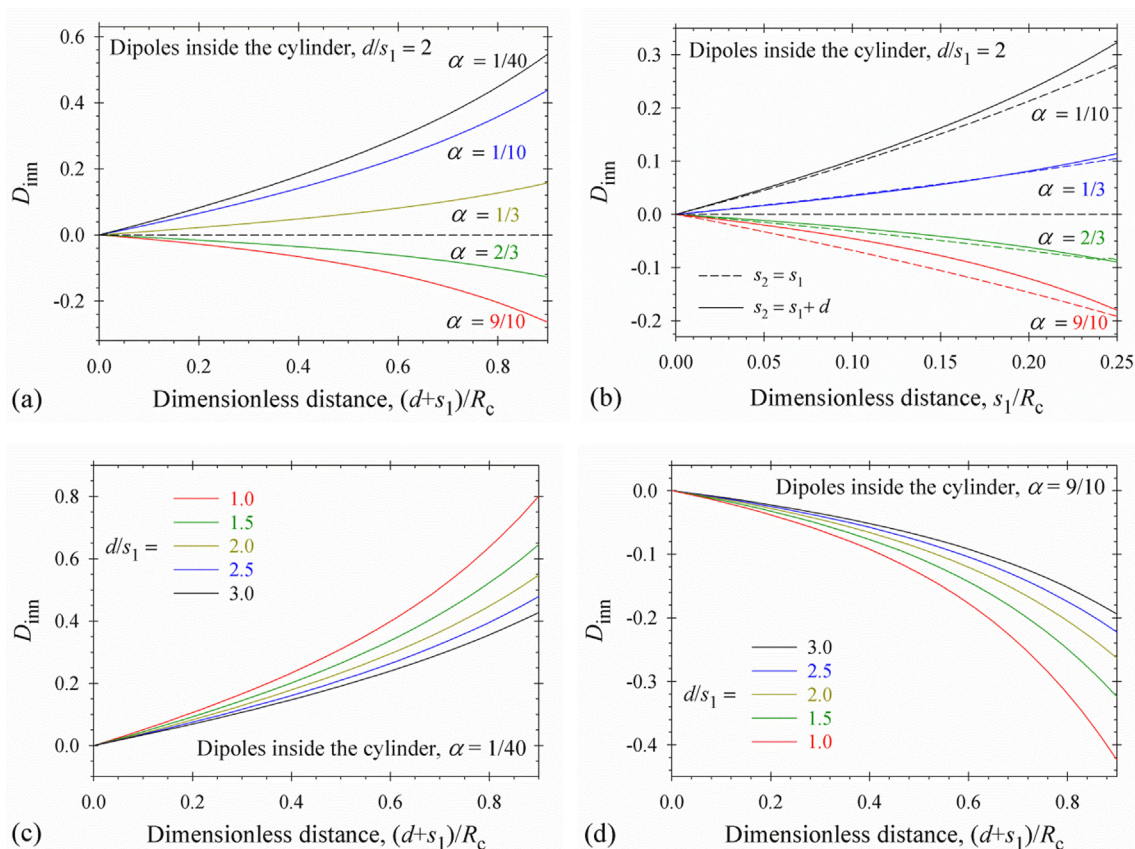


Fig. 7. Dipole interaction energy for a dipole inside a cylindrical dielectric phase – dependence of D_{inn} on the cylindrical radius R_c and the dipole positions and orientations: a) $d = 2s_1$, $s_2 = s_1 + d$, and different ratios between dielectric constants; b) $d = 2s_1$, perpendicular and parallel dipole orientations, and different values of α ; c) $\alpha = 1/40$ and $\alpha = 9/10$ for $s_2 = s_1 + d$, i.e. perpendicular orientation, and different values of the dipole lengths.

correlates with experimental observations. It is interesting to note that all molecular parameters for pentaerythylene dodecyl ester ($C_{12}E_5$) and DDAO are identical [15,26] and the same is observed for $C_{14}E_5$ and TDAO. The only difference from the viewpoint of molecular thermodynamics is the appearance of the dipole free energy for the zwitterionic surfactants. The contribution of f_{dip} changes dramatically the scission energy and growth of micelles: $E_{\text{sc}} = 23.7 k_B T$ for $C_{12}E_5$ [15] vs $10.04 k_B T$ for DDAO; $E_{\text{sc}} = 28.4 k_B T$ for $C_{14}E_5$ [26] vs $16.15 k_B T$ for TDAO. Moreover, the values of mean aggregation number calculated by the model of Nagarajan and Ruckenstein [30] for the two examples are: i) 15,700 and 24,900 for 175 and 440 mM DDAO vs experimental data of 98 and 103, respectively; ii) 23,300 and 39,400 for 3.5 and 10 mM TDAO vs experimental data of 126 and 178.

To predict the mean aggregation number and the size distribution of micelles at arbitrary values of the scission energy, the general molecular thermodynamic approach should be applied. The single component surfactant solution contains X_1 mole fraction of surfactant molecules in monomeric form and X_n mole fraction of aggregates that are composed of n surfactant molecules ($n > 1$). The minimization of the total free energy of the solution under the mass balance condition:

$$X_S = X_1 + \sum_{n>1} nX_n \quad (16)$$

leads to the well-known relationship [30]:

$$X_n = [X_1 \exp(-\frac{f_n^o - \mu_1^o}{k_B T})]^n \quad (n > 1) \quad (17)$$

Here μ_1^o is the standard chemical potential of free monomers in an aqueous solution and f_n^o is the free energy per surfactant mole-

cule in a micelle of aggregation number n . Hence the mean mass aggregation number, n_M , can be calculated from the expression [45]:

$$n_M = \frac{1}{X_S - X_1} \sum_{n>1} n^2 X_n \quad (18)$$

For a given optimal shape of the aggregate composed of n surfactant molecules, the free energy, f_n^o , is a sum of the considered contributions and the energy difference in the exponent in the right-hand side of Eq. (17) is equal to $f_n^o - \mu_1^o = -(\mu_s^o - \mu_m^o) + \Delta f$, where $\Delta f \equiv \Delta f_\sigma + \Delta f_{\text{hs}} + \Delta f_{\text{conf}} + \Delta f_{\text{dip}}$. The difference between the standard chemical potentials, $\mu_1^o - \mu_m^o$, is independent of the shapes of aggregates. Therefore, the optimal spherocylindrical micelle shape for fixed aggregation number n corresponds to the minimum of $n\Delta f = n_s(\Delta f)_s + (n - n_s)(\Delta f)_c$ under all geometrical restrictions. Fig. 9 shows the dependence of the optimal radius of the spheres, the spherical part of the elongated shapes, and spherical endcaps, R_s , on the aggregation number. One sees that the micelles are spherical for aggregation numbers smaller than those corresponding to $R_s = l$: 30 vs 56 for DDAO; 35 vs 73 for TDAO (left dashed lines in Fig. 9). In the transition region ($30 < n \leq 92$ for DDAO and $35 < n \leq 106$ for TDAO), the optimal shapes of micelles are two truncated spheres with radius R_s and R_c is the radius of the cross sectional circle (Fig. 9). In all cases, the radii R_s are smaller than the corresponding extended length, l . Further increase of the aggregation number ($n > 92$ for DDAO and $n > 106$ for TDAO) leads to the formation of spherocylindrical micelles (with a small decrease of R_s and R_c) up to very large aggregation numbers, for which R_s and R_c remain constants and the aggregates grow only because of the increase of the lengths of their cylindrical parts.

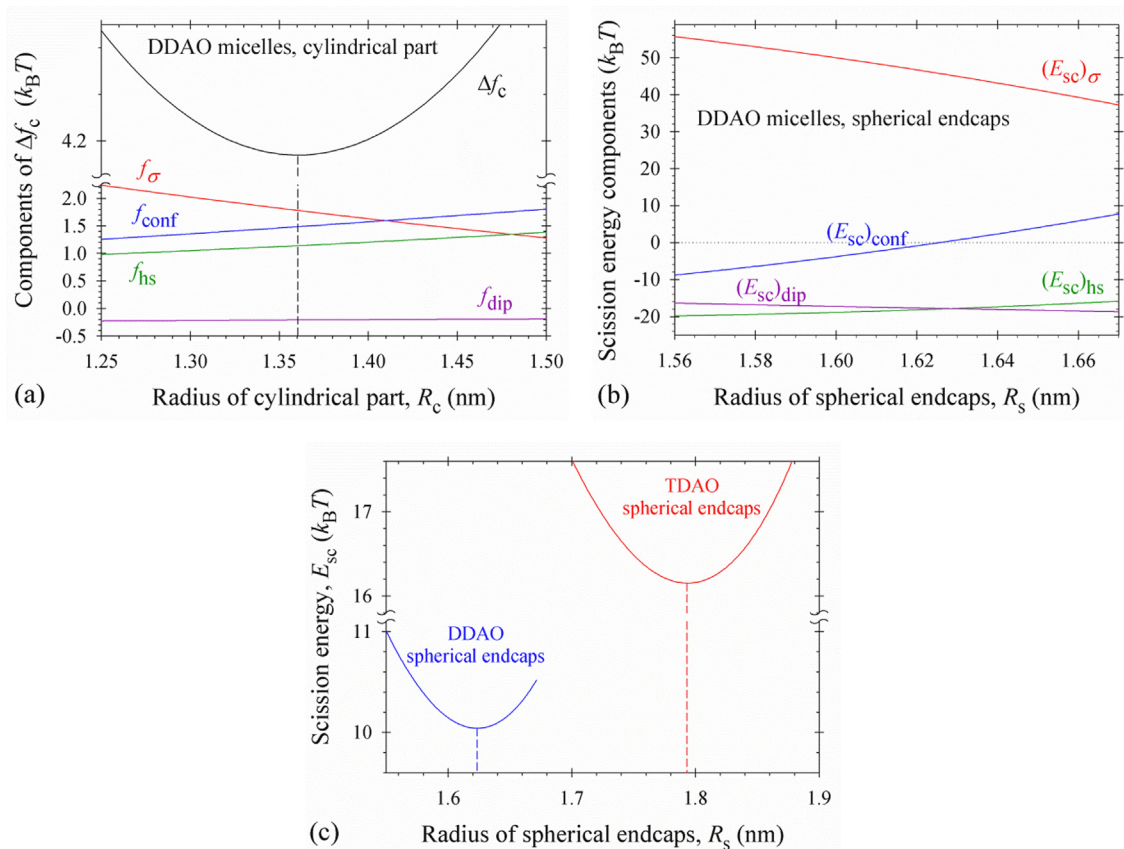


Fig. 8. Plots of: (a) components of the total free energy of a surfactant molecule in the micelle cylindrical part vs R_c ; (b) scission energy components vs R_s for the micelle spherical endcaps for DDAO; (c) E_{sc} vs R_s for DDAO and TDAO micelle endcaps. The vertical dashed lines correspond to the positions of the respective minima.

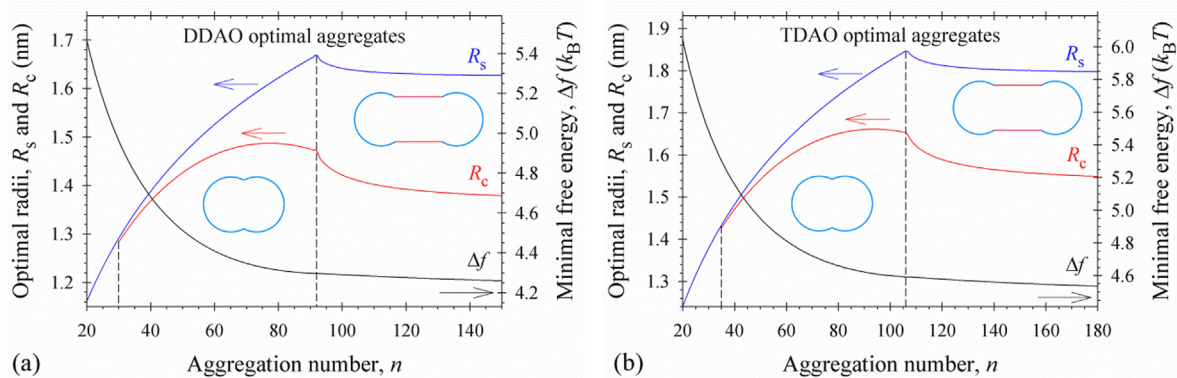


Fig. 9. Plots of the optimal radii, R_s and R_c , and the minimal free energy, Δf , vs aggregation number n : (a) DDAO micelles; (b) TDAO micelles. The vertical dashed lines show the transition from spheres to elongated shapes and subsequently to spherocylindrical micelles.

The asymptotic values of R_s and R_c for large aggregation numbers correspond exactly to those illustrated in Fig. 8a, 8c, and D3 in Appendix D and used to calculate the respective scission energy.

The difference between the standard chemical potentials, $\mu_1^0 - \mu_m^0$, is needed to predict the size distribution of micelles and the critical micelle concentration, X_{CMC} , while the geometry of the optimal aggregates and Δf (Fig. 9) are independent of $\mu_1^0 - \mu_m^0$. The CMC can be obtained by constructing a plot of X_1 against the total surfactant concentration, X_S (see Fig. D4 in Appendix D). In the molecular thermodynamics, the CMC has been estimated as that value of X_1 for which the concentration of the singly dispersed surfactant molecules is equal to that of surfactant present in the form of aggregates [30,46–48]. The experimental observations

show that the CMC of DDAO at room temperature changes from 0.7 mM to 2.4 mM depending on the solution pH [18,49–52]. Using the experimental value of the CMC for DDAO in a zwitterionic form of 1.70 mM, we obtained that the difference between standard chemical potentials is equal to 14.49 $k_B T$ (see Fig. D4 in Appendix D). The lower value of $\mu_1^0 - \mu_m^0$ is because of the contribution of the constant dipole interaction energy, Eq. (1), in the standard chemical potential. Above the CMC of DDAO, the concentration of monomers slightly increases from 1.70 mM to 1.78 mM with the rise of the total surfactant concentration. The experimental data for the CMC of TDAO [23,53,54] show the variation of the CMC with pH from 0.15 mM to 0.25 mM. For the CMC value of TDAO in a zwitterionic form (0.15 mM), we calculated that the standard

chemical potential difference is equal to $17.21 k_B T$ (see Fig. D4 in Appendix D). Above the CMC of TDAO, the respective concentration of monomers increases from 0.15 mM to 0.157 mM with the rise of the total surfactant concentration. The difference between the standard chemical potentials of TDAO and DDAO is $2.72 k_B T$, which corresponds to $1.36 k_B T$ per one CH_2 group [30]. Finally, all physicochemical parameters for DDAO and TDAO molecules needed for a quantitative prediction of the number distribution of aggregates and the mean aggregation number, n_M , are defined.

Fig. 10 shows the calculated mass distributions of aggregates, nX_n , for DDAO and TDAO micellar solutions. The positions of maximums of nX_n depend insignificantly on the total surfactant concentrations, X_S – they are at aggregation numbers 90 for DDAO and 105 for TDAO. The number of molecules incorporated in the n -th micellar aggregate decreases considerably with the rise of aggregation number n for DDAO micelles (Fig. 10a) even at very large total surfactant concentrations (1 M). Hence the total amount of surfactant molecules incorporated in the long spherocylindrical micelles for DDAO is small and the mean aggregation number, n_M , increases slightly with the rise of concentration X_S . In contrast, the mass distributions of aggregates for TDAO micellar solutions (Fig. 10b) have pronounced long tails seen for $n > 105$. The total number of molecules incorporated in these aggregates increases with the rise of surfactant concentration for relatively low values of X_S (from 2 to 50 mM). As a result, the mean mass aggregation number considerably increases for not so large TDAO total concentrations.

The first study of the aggregation number of zwitterionic DDAO micelles occurred in 1962 [55]; the reported value of $n_M = 76$ is smaller than the measured lately values of $n_M = 103$ – 110 given in [18,19,49]. The results from the molecular dynamics simulations of the interfacial and structural properties of DDAO micelles show that the micelles are generally ellipsoidal in shape with an axial ratio of about 1.4 [56]. Recently, the size and aggregation number of DDAO micelles for a wide range of surfactant concentration have been studied using a combination of small angle neutron scattering and Fourier-transform infrared spectroscopy [22]. Fig. 11a shows experimental data for n_M [22] and the calculated theoretical predictions from the proposed molecular thermodynamic approach without adjustable parameters. It is remarkable that n_M changes only from 90 to 115 with the rise of DDAO total surfactant concentration up to 1.3 M. For comparison, the mean mass aggregation numbers of C_{12}E_5 [15] versus surfactant concentration are included in Fig. 11a. One sees that for 100 mM surfactant concentration, the aggregation number of C_{12}E_5 micelles is >150 times greater than that of DDAO.

The mean aggregation numbers and sizes of TDAO micelles are reported in the literature [23,42,57,58]. The relationship between the growth of rodlike TDAO micelles and the viscoelastic properties of TDAO micellar solutions has been systematically studied in Ref. [59]. The experimental data for n_M vs surfactant concentration [57] are shown in Fig. 11b. As expected, the micellar aggregation number gradually increases with X_S , see Fig. 11b. Even for low concentration (53.4 mM), the experimental value of $n_M = 315 \pm 35$ has

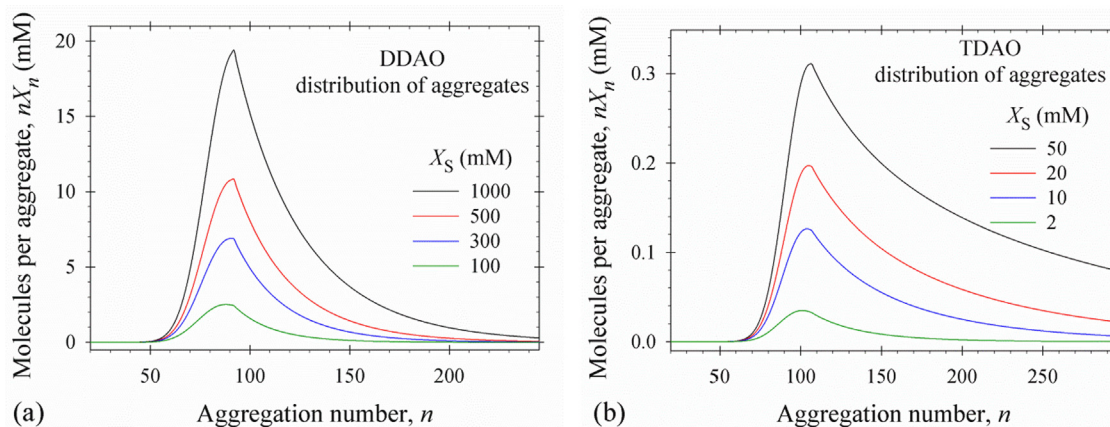


Fig. 10. Plots of the mass distribution of aggregates, nX_n , vs the aggregation number, n , for different total surfactant concentrations X_S : (a) DDAO micelles; (b) TDAO micelles.

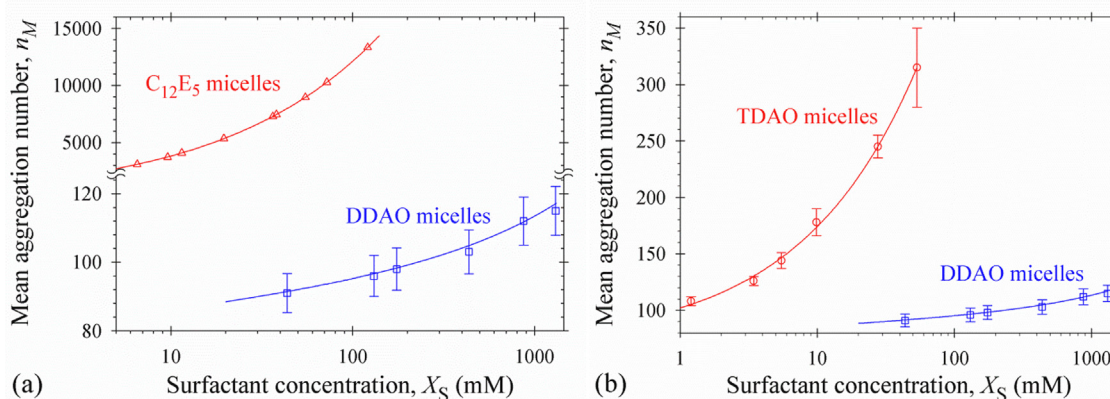


Fig. 11. Experimental data for the mean aggregation numbers, n_M , vs molecular thermodynamic theory (solid lines): (a) DDAO micellar solutions, experimental data from Ref. [22], and C_{12}E_5 micellar solutions [15]; (b) TDAO micellar surfactant solutions, experimental data from Ref. [57].

been reported. The solid lines in Fig. 11 are drawn without adjustable parameters – the theoretical predictions coincide with experimental data in the frame of experimental errors.

5. Conclusions

The viscoelastic properties of a wide range of micellar solutions are related to the growth of rodlike and wormlike micelles, characterized by the scission excess energy, E_{sc} , between their spherical endcaps and cylindrical parts. In our previous studies [15,16,25–27], E_{sc} was calculated in the frame of molecular thermodynamics for nonionic and ionic surfactants with and without added electrolytes (salts) and their mixtures. Excellent agreement was achieved between the proposed therein theory and experiments. All molecular parameters of many nonionic and zwitterionic surfactants are practically identical. It is not clear, why these nonionic surfactants have lower values of the critical micelle concentration (CMC), considerably larger scission energy, micellar sizes, and respectively pronounced viscoelastic behavior of their solutions [15] compared to the similar (from the viewpoint of their molecular parameters) zwitterionic surfactants [22]. The present paper is based on the detailed theory of micelle dipole interaction free energy, f_{dip} , and its crucial importance on the CMC, micellar size distribution, and E_{sc} of zwitterionic surfactant solutions, see Section 4.

For this goal, we first derived the exact expressions for the interaction energy between a single charge and nonpolar dielectric phase (e.g. micellar hydrocarbon core) based on the exact solutions of the respective electrostatic problems in spherical and cylindrical dielectric media [32,34] (Section 2). Applying the superposition principle in Section 3, the exact formulae for the interaction energy between a dipole and nonpolar dielectric phase are obtained. The reported results are valid for dipole's arbitrary lengths, orientations and distances to the dividing cylindrical and spherical boundaries between the dielectric phases with different dielectric constants. The detailed numerical results (Figs. 4–7) showed the effects of all studied system parameters on the dipole interaction free energy, f_{dip} . For dipoles outside the confined nonpolar phase (the case corresponding to zwitterionic surfactant micelles), the dipole interaction energy decreases with the rise of the radius of curvature, the dipole length and the difference between the dielectric constants of phases. These effects are more pronounced for spheres compared to cylinders. In the case of dipoles inside the confined dielectric phase (the case corresponding to inverse emulsions), the trends are exactly the opposite. Because of the generality of the exact solutions and the formal analogy between electrostatics and magnetostatics, the obtained results are also applicable for magnetically polarizable spheres and cylinders. They could be used for modeling a broad class of physicochemical problems.

The new analytical model for f_{dip} without any adjustable parameters (Section 4) allows one to obtain a perfect agreement between the experiments and the molecular thermodynamic description of zwitterionic micellar solutions. The calculated optimal micellar shape parameters (Fig. 9a), size distributions (Fig. 10a), and mean mass aggregation numbers, n_M (Fig. 11a) for DDAO micellar solutions showed the formation of spherocylindrical micelles with a narrow distribution around aggregation number of 90 and a small increase of n_M from 90 to 115 with the considerable rise of the total surfactant concentration up to 1.3 M as observed experimentally [22]. The longer hydrocarbon tail of TDAO leads to larger radii of the spherical endcaps and cylindrical parts of optimal micelles (Fig. 9b), a peak of the micellar size distribution at aggregation number of 105, followed by a long tail in the micellar size distribu-

tion even at >25 times lower total surfactant concentrations (Fig. 10b). As a result, the mean aggregation numbers of zwitterionic TDAO micelles significantly increase with surfactant concentrations (Fig. 11b) even at 50 mM [57].

The present molecular thermodynamic approach can be further extended to explain the effects of different pHs and salt concentrations on the size and distribution of zwitterionic surfactants [6,49,51,59] and their synergistic mixing with ionic surfactants [12–14,17,22,24,52]. The obtained results could be of interest to the theoreticians to build up adequate models and simulations of complex fluids and for the experimentalists to plan their study and develop new formulations.

CRedit authorship contribution statement

Krassimir D. Danov: Conceptualization, Software, Formal analysis, Supervision, Writing – original draft. **Krastanka G. Marinova:** Conceptualization, Methodology. **Gergana M. Radulova:** Investigation, Data curation. **Mihail T. Georgiev:** Investigation, Data curation.

Data availability

Data will be made available on request.

Declaration of Competing Interest

The authors declare that they have no known competing financial interests or personal relationships that could have appeared to influence the work reported in this paper.

Acknowledgements

The authors are grateful to the project № КП-06-ПН 49/5 with the Bulgarian Science Fund (FNI-MON) for the financial support, and to Project CoE “National center of mechatronics and clean technologies” BG05M2OP001-1.001-0008 of the Operational Programme “Science and Education for Smart Growth 2014 – 2020” for the used equipment to determine surface tension isotherm and micellar size and aggregation numbers.

Appendix A. Supplementary material

Supplementary data to this article can be found online at <https://doi.org/10.1016/j.jcis.2022.07.087>.

References

- [1] D. Balzer, S. Varwig, M. Wehrauch, Viscoelasticity of personal care products, *Colloid Surf. A* 99 (1995) 233–246, [https://doi.org/10.1016/0927-7757\(95\)03144-3](https://doi.org/10.1016/0927-7757(95)03144-3).
- [2] J. Yang, Viscoelastic wormlike micelles and their applications, *Curr. Opin. Colloid Interface Sci.* 7 (2002) 276–281, [https://doi.org/10.1016/S1359-0294\(02\)00071-7](https://doi.org/10.1016/S1359-0294(02)00071-7).
- [3] R. Zana, E. Kaler (Eds.), *Giant Micelles. Properties and Applications*, Taylor and Francis, New York, 2007, <https://doi.org/10.1201/9781420007121>.
- [4] C.A. Dreiss, Y. Feng (Eds.), *Wormlike Micelles: Advances in Systems, Characterization and Applications*, RSC Publishing, 2017, <https://doi.org/10.1039/9781782629788>.
- [5] E.J. Nodoushan, T. Yi, Y.J. Lee, N. Kim, Wormlike micellar solutions, beyond the chemical enhanced oil recovery restrictions, *Fluids* 4 (2019) 173, <https://doi.org/10.3390/fluids4030173>.
- [6] H. Hoffmann, A. Rauscher, M. Gradzielski, S.F. Schulz, Influence of ionic surfactants on the viscoelastic properties of zwitterionic surfactant solutions, *Langmuir* 8 (1992) 2140–2146, <https://doi.org/10.1021/la00045a013>.
- [7] S. Hoffmann, H. Hoffmann, Shear-induced micellar structures in ternary surfactant mixtures: the influence of the structure of the micellar interface, *J. Phys. Chem. B* 102 (1998) 5614–5624, <https://doi.org/10.1021/jp980339w>.

- [8] N. Dan, K. Shimoni, V. Pata, D. Danino, Effect of mixing on the morphology of cylindrical micelles, *Langmuir* 22 (2006) 9860–9865, <https://doi.org/10.1021/la061254m>.
- [9] K. Imanishi, Y. Einaga, Wormlike micelles of polyoxyethylene alkyl ether mixtures $C_{10}E_5+C_{14}E_5$ and $C_{14}E_5+C_{14}E_7$: hydrophobic and hydrophilic chain length dependence of the micellar characteristics, *J. Phys. Chem. B* 111 (2007) 62–73, <https://doi.org/10.1021/jp065317l>.
- [10] D. Danino, Cryo-TEM of soft molecular assemblies, *Curr. Opin. Colloid Interface Sci.* 17 (2012) 316–329, <https://doi.org/10.1016/j.cocis.2012.10.003>.
- [11] M. Kamada, S. Shimizu, K. Aramaki, Manipulation of the viscosity behavior of wormlike micellar gels by changing the molecular structure of added perfumes, *Colloid Surf. A* 458 (2014) 110–116, <https://doi.org/10.1016/j.colsurfa.2014.01.003>.
- [12] S. Róžańska, Rheology of wormlike micelles in mixed solutions of cocoamidopropyl betaine and sodium dodecylbenzenesulfonate, *Colloid Surf. A* 482 (2015) 394–402, <https://doi.org/10.1016/j.colsurfa.2015.06.045>.
- [13] Z. Mitrinova, S. Tcholakova, N. Denkov, Control of surfactant solution rheology using medium-chain cosurfactants, *Colloid Surf. A* 537 (2018) 173–184, <https://doi.org/10.1016/j.colsurfa.2017.10.018>.
- [14] V.I. Yavrukova, G.M. Radulova, K.D. Danov, P.A. Kralchevsky, H. Xu, Y.W. Ung, J. T. Petkov, Rheology of mixed solutions of sulfonated methyl esters and betaine in relation to the growth of giant micelles and shampoo applications, *Adv. Colloid Interface Sci.* 275 (2020), <https://doi.org/10.1016/j.cis.2019.102062>.
- [15] K.D. Danov, P.A. Kralchevsky, S.D. Stoyanov, J.L. Cook, I.P. Stott, E.G. Pelan, Growth of wormlike micelles in nonionic surfactant solutions: Quantitative theory vs. experiment, *Adv. Colloid Interface Sci.* 256 (2018) 1–22, <https://doi.org/10.1016/j.cis.2018.05.006>.
- [16] K.D. Danov, P.A. Kralchevsky, R.D. Stanimirova, S.D. Stoyanov, J.L. Cook, I.P. Stott, Analytical modeling of micelle growth. 4. Molecular thermodynamics of wormlike micelles from ionic surfactants: Theory vs. experiment, *J. Colloid Interf. Sci.* 584 (2021) 561–581, <https://doi.org/10.1016/j.jcis.2020.10.004>.
- [17] M. Pleines, W. Kunz, T. Zemb, D. Benczédi, W. Fieber, Molecular factors governing the viscosity peak of giant micelles in the presence of salt and fragrances, *J. Colloid Interf. Sci.* 537 (2019) 682–693, <https://doi.org/10.1016/j.jcis.2018.11.072>.
- [18] M. Kakitani, T. Imae, M. Furusaka, Investigation of mixed micelles of dodecyltrimethylamine oxide and sodium dodecyl sulfate by SANS: Shape, size, charge, and interaction, *J. Phys. Chem.* 99 (1995) 16018–16023, <https://doi.org/10.1021/j100043a048>.
- [19] D.J. Barlow, M.J. Lawrence, T. Zuberi, S. Zuberi, R.K. Heenan, Small-angle neutron-scattering study on the nature of the incorporation of polar oils into aggregates of N, N-Dimethyldodecylamine-N-oxide, *Langmuir* 16 (2000) 10398–10403, <https://doi.org/10.1021/la0002233>.
- [20] N.C. Christov, N.D. Denkov, P.A. Kralchevsky, K.P. Ananthapadmanabhan, A. Lips, Synergistic sphere-to-rod micelle transition in mixed solutions of sodium dodecyl sulfate and cocoamidopropyl betaine, *Langmuir* 20 (2004) 565–571, <https://doi.org/10.1021/la035717p>.
- [21] S.K. Singh, M. Bajpai, V.K. Tyagi, Amine oxides: A review, *J. Oleo Sci.* 55 (2006) 99–119, <https://doi.org/10.5650/jos.55.99>.
- [22] S. Khodaparast, W.N. Sharratt, G. Tyagi, R.M. Dalgliesh, E.S.J. Robles, J.T. Cabral, Pure and mixed aqueous micellar solutions of sodium dodecyl sulfate (SDS) and dimethyldodecyl amine oxide (DDAO): Role of temperature and composition, *J. Colloid Interf. Sci.* 582 (2021) 1116–1127, <https://doi.org/10.1016/j.jcis.2020.08.002>.
- [23] H. Maeda, Y. Kanakubo, M. Miyahara, R. Kakehashi, V. Garamus, J.S. Pedersen, Effects of protonation on tetradecyldimethylamine oxide micelles, *J. Phys. Chem. B* 104 (2000) 6174–6180, <https://doi.org/10.1021/jp993380n>.
- [24] W. Zhang, J. Mao, X. Yang, H. Zhang, B. Yang, Z. Zhang, Y. Zhang, J. Zhao, Development of a stimuli-responsive gemini zwitterionic viscoelastic surfactant for self-diverting acid, *J. Surfactant Deterg.* 22 (2019) 535–547, <https://doi.org/10.1002/jsde.12267>.
- [25] K.D. Danov, P.A. Kralchevsky, S.D. Stoyanov, J.L. Cook, I.P. Stott, Analytical modeling of micelle growth. 1. Chain-conformation free energy of binary mixed spherical, wormlike and lamellar micelles, *J. Colloid Interf. Sci.* 547 (2019) 245–255, <https://doi.org/10.1016/j.jcis.2019.03.105>.
- [26] K.D. Danov, P.A. Kralchevsky, S.D. Stoyanov, J.L. Cook, I.P. Stott, Analytical modeling of micelle growth. 2. Molecular thermodynamics of mixed aggregates and scission energy in wormlike micelles, *J. Colloid Interf. Sci.* 551 (2019) 227–241, <https://doi.org/10.1016/j.jcis.2019.05.017>.
- [27] K.D. Danov, P.A. Kralchevsky, S.D. Stoyanov, J.L. Cook, I.P. Stott, Analytical modeling of micelle growth. 3. Electrostatic free energy of ionic wormlike micelles – Effects of activity coefficients and spatially confined electric double layers, *J. Colloid Interf. Sci.* 581 (2021) 262–275, <https://doi.org/10.1016/j.jcis.2020.07.059>.
- [28] M. Pleines, W. Kunz, T. Zemb, Understanding and prediction of the clouding phenomenon by spontaneous and packing concepts, *J. Colloid Interf. Sci.* 22 (2019) 1011–1021, <https://doi.org/10.1002/jsde.12273>.
- [29] W. Fieber, A. Scheklaikov, W. Kunz, M. Pleines, D. Benczédi, T. Zemb, Towards a general understanding of the effects of hydrophobic additives on the viscosity of surfactant solutions, *J. Mol. Liq.* 329 (2021), <https://doi.org/10.1016/j.molliq.2021.115523>.
- [30] R. Nagarajan, E. Ruckenstein, Theory of surfactant self-assembly: A predictive molecular thermodynamic approach, *Langmuir* 7 (1991) 2934–2969, <https://doi.org/10.1021/la00060a012>.
- [31] L.D. Landau, E.M. Lifshitz, L.P. Pitaevskii, *Electrodynamics of Continuous Media*, Elsevier Butterworth-Heinemann, Oxford, 2004.
- [32] D.V. Redžić, M.S.A. Eldakli, M.D. Redžić, Image charge inclusion in the dielectric sphere revisited, *Eur. J. Phys.* 33 (2012) 1751–1759, <https://doi.org/10.1088/0143-0807/33/6/1751>.
- [33] D.V. Redžić, S.S. Redžić, Image charge inclusions in the prolate dielectric spheroid, *J. Phys. D: Appl. Phys.* 38 (2005) 3991–3994, <https://doi.org/10.1088/0022-3727/38/21/025>.
- [34] S.T. Cui, Electrostatic potential in cylindrical dielectric media using the image charge method, *Mol. Phys.* 104 (2006) 2993–3001, <https://doi.org/10.1080/00268970600926647>.
- [35] J. Selvaggi, S. Salon, M.V.K. Chari, An application of toroidal functions in electrostatics, *Am. J. Phys.* 75 (2007) 724–727, <http://link.aip.org/link/doi/10.1119/1.2737473>.
- [36] C. DeW Van Siclen, Method of images and electrostatic screening by a polarized dielectric sphere, *Am. J. Phys.* 56 (1988) 1142–1143, <https://doi.org/10.1119/1.15741>.
- [37] N. Daneshfar, N. Moradbeigi, Solution for the electrostatic potential and field distribution in cylindrical core-shell nanoparticles using the image charge method, *AIP Adv.* 5 (2015), <https://doi.org/10.1063/1.4938255> 127214.
- [38] D.V. Redžić, S.S. Redžić, Image current inclusion in the permeable sphere, *Eur. J. Phys.* 27 (2006) 787–792, <https://doi.org/10.1088/0143-0807/27/4/010>.
- [39] J. Selvaggi, S. Salon, M.V.K. Chari, Employing toroidal harmonics for computing the magnetic field from axially magnetized multipole cylinders, *IEEE Trans. Magn.* 46 (2010) 3715–3723, <https://doi.org/10.1109/TMAG.2010.2051558>.
- [40] M. Abramowitz, I. Stegun (Eds.), *Handbook of Mathematical Functions: With Formulas, Graphs, and Mathematical Tables*, 9th, revised edition., *Dover Books of Mathematics*, Dover Publications, New York, 1965.
- [41] T. Ohto, J. Hunger, E.H.G. Backus, W. Mizukami, M. Bonn, Y. Nagata, Trimethylamine-N-oxide: Its hydration structure, surface activity, and biological function, viewed by vibrational spectroscopy and molecular dynamics simulations, *Phys. Chem. Chem. Phys.* 18 (2017) 6909–6920, <https://doi.org/10.1039/c6cp07284d>.
- [42] J. Hunger, K.J. Tielrooij, R. Buchner, M. Bonn, H.J. Bakker, Complex formation in aqueous trimethylamine-N-oxide (TMAO) solutions, *J. Phys. Chem. B* 116 (2012) 4783–4795, <https://doi.org/10.1021/jp212542q>.
- [43] C. Wohlfarth, Static Dielectric Constants of Pure Liquids and Binary Liquid Mixtures, Supplement to Vol. IV/17, M.D. Lechner (Ed.), *Landolt-Börnstein: Numerical Data and Functional Relationships in Science and Technology*, Springer, 2015.
- [44] P. Mukerjee, Hydrophobic and electrostatic interactions in ionic micelles. Problems in calculating monomer contributions to the free energy, *J. Phys. Chem.* 73 (1969) 2054–2056, <https://doi.org/10.1021/j100726a069>.
- [45] P.J. Missel, N.A. Mazer, G.B. Benedek, C.Y. Young, M.C. Carey, Thermodynamic analysis of the growth of sodium dodecyl sulfate micelles, *J. Phys. Chem.* 84 (1980) 1044–1057, <https://doi.org/10.1021/j100446a021>.
- [46] S. Puvvada, D. Blankschtein, Molecular-thermodynamic approach to predict micellization, phase behavior and phase separation of micellar solutions: I. Application to nonionic surfactants, *J. Chem. Phys.* 92 (1990) 3710–3724, <https://doi.org/10.1063/1.457829>.
- [47] L. Moreira, A. Firoozabadi, Molecular thermodynamic modeling of specific ion effects on micellization of ionic surfactants, *Langmuir* 26 (2010) 15177–15191, <https://doi.org/10.1021/la102536y>.
- [48] S.V. Koroleva, A.I. Victorov, Modeling of the effects of ion specificity on the onset and growth of ionic micelles in a solution of simple salts, *Langmuir* 30 (2014) 3387–3396, <https://doi.org/10.1021/la4044845y>.
- [49] H. Maeda, S. Muroi, R. Kakehashi, Effects of ionic strength on the critical micelle concentration and the surface excess of dodecyltrimethylamine oxide, *J. Phys. Chem. B* 101 (1997) 7378–7382, <https://doi.org/10.1021/jp9633815>.
- [50] Y. Imaishi, R. Kakehashi, T. Nezu, H. Maeda, Dodecyltrimethylamine oxide micelles in solutions without added salt, *J. Colloid Interf. Sci.* 197 (1998) 309–316, <https://doi.org/10.1006/jcis.1997.5242>.
- [51] V. Lair, S. Bouguerra, M. Turmine, P. Letellier, Thermodynamic study of the protonation of dimethyldodecylamine N-oxide micelles in aqueous solution at 298 K. Establishment of a theoretical relationship linking critical micelle concentrations and pH, *Langmuir* 20 (2004) 8490–8495, <https://doi.org/10.1021/la049067g>.
- [52] K.D. Thompson, E.P. Danielson, K.N. Peterson, N.O. Nocoovski, J.T. Boock, J.A. Berberich, The amphoteric surfactant N, N-dimethyldodecylamine N-oxide unfolds β -lactoglobulin above the critical micelle concentration, *Langmuir* 38 (2022) 4090–4101, <https://doi.org/10.1021/acs.langmuir.2c00172>.
- [53] J.A. Zimmerman, R.L. Schnaare, Predicting the critical micelle concentration in a pH-mediated ternary-surfactant mixtures using the regular solution approximation, *J. Colloid Interf. Sci.* 220 (1999) 75–80, <https://doi.org/10.1006/jcis.1999.6499>.
- [54] H. Maeda, A thermodynamic analysis of the hydrogen ion titration of micelles, *J. Colloid Interf. Sci.* 263 (2003) 277–287, [https://doi.org/10.1016/S0021-9797\(03\)00237-6](https://doi.org/10.1016/S0021-9797(03)00237-6).
- [55] K.W. Herrmann, Non-ionic-cationic micellar properties of dimethyldodecylamine oxide, *J. Phys. Chem.* 66 (1962) 295–300, <https://doi.org/10.1021/j100808a025>.
- [56] C.D. Lorenz, C.-M. Hsieh, C.A. Dreiss, M.J. Lawrence, Molecular dynamics simulations of the interfacial and structural properties of dimethyldodecylamine-N-oxide micelles, *Langmuir* 27 (2011) 546–553, <https://doi.org/10.1021/la1031416>.

- [57] N. Gorski, J. Kalus, Determination of the structure of tetradecyldimethylaminoxide micelles in water by small-angle-neutron-scattering, *J. Phys. Chem. B* 101 (1997) 4390–4393, <https://doi.org/10.1021/jp9704776>.
- [58] H. Pils, H. Hoffmann, S. Hofmann, J. Kalus, A.W. Kencono, P. Lindner, W. Ulbicht, Shape investigation of mixed micelles by small angle neutron scattering, *J. Phys. Chem.* 97 (1993) 2745–2754, <https://doi.org/10.1021/j100113a042>.
- [59] H. Maeda, A. Yamamoto, M. Souda, H. Kawasaki, K.S. Hossain, N. Nemoto, M. Almgren, Effect of protonation on the viscoelastic properties of tetradecyldimethyl amine oxide micelles, *J. Phys. Chem. B* 105 (2001) 5411–5418, <https://doi.org/10.1021/jp0101155>.

Supplementary Material

for the article

Analytical modeling of micelle growth. 5. Molecular thermodynamics of micelles from zwitterionic surfactants

Authors: K.D. Danov, K.G. Marinova, G.M. Radulova, M.T. Georgiev

Here, the reference numbers are different from those in the main text; the list of cited references is given at the end of the present Supplementary Material.

Appendix A. Planar geometry

In the case of planar geometry, the solution of the electrostatic problem for charge q at distance s from the dividing surface between two dielectric phases (Fig. A1) is well-known in the literature [1]. In Cartesian coordinate system, $Oxyz$, the position of the interface is defined by $z = 0$, the original charge q is placed at the point $z = s$, so that the position of the image charge, q_n , is at $z = -s$, see Fig. A1. The relative dielectric constants of the phases are ε and ε_n , respectively, and the original charge is placed in the phase with dielectric constant ε . For simplicity, the dielectric phase with dielectric constant ε_n is hereinafter referred to as the nonpolar phase and that with ε – as the dielectric phase.

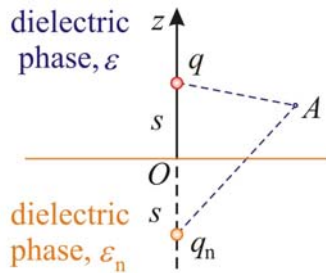


Fig. A1. Schematic presentation of a charge q at distance s from the dividing surface between two phases with dielectric constants ε and ε_n . q_n is the image charge of q .

If ε_0 is the dielectric permittivity of vacuum and φ is the electrostatic potential at an arbitrary point $A(x, y, z)$ in the phase where the charge is positioned, then the exact solution of the electrostatic problem in Cartesian coordinates (Fig. A1) reads:

$$\varphi = \frac{q}{4\pi\varepsilon_0\varepsilon} [x^2 + y^2 + (z-s)^2]^{-1/2} + \frac{q_n}{4\pi\varepsilon_0\varepsilon} [x^2 + y^2 + (z+s)^2]^{-1/2} \quad (\text{A1})$$

The image charge, q_n , is related to the original charge, q , by the following expression:

$$q_n = \frac{\varepsilon - \varepsilon_n}{\varepsilon + \varepsilon_n} q \quad (\text{A2})$$

Hence, the expression for the electrostatic interaction energy, u_c^0 , between the charge and the nonpolar phase reads:

$$u_c^0 = \frac{q^2}{4\pi\varepsilon_0\varepsilon} \frac{\varepsilon - \varepsilon_n}{\varepsilon + \varepsilon_n} \frac{1}{2s} \quad (\text{A3})$$

The dimensionless interaction energy is convenient to be presented in terms of the Bjerrum length, L_B , and the ratio between the dielectric constants, α :

$$L_B \equiv \frac{e^2}{4\pi\varepsilon_0\varepsilon k_B T} \quad \text{and} \quad \alpha \equiv \frac{\varepsilon_n}{\varepsilon + \varepsilon_n} < 1 \quad (\text{A4})$$

where e is the elementary charge, T is the temperature, k_B is the Boltzmann constant, and $z_c \equiv q/e$ is the ion valence. For water at 25 °C, the Bjerrum length, L_B , is equal to 7.1 Å. Thus Eq. (A3) acquires the following final form:

$$\frac{u_c^0}{k_B T} = (1 - 2\alpha) z_c^2 \frac{L_B}{2s} \quad (\text{A5})$$

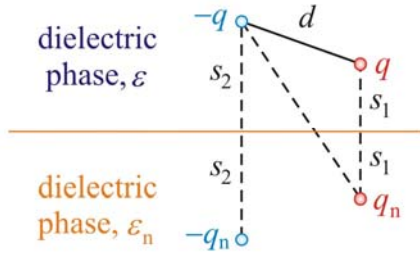


Fig. A2. A dipole close to the dividing surface between two dielectric phases: d is the dipole length; s_1 and s_2 are the closest distances from the charges to the interface.

The dipole consists of two opposite charges (q and $-q$) with dipole length d (Fig. A2). The closest distances from the dipole charges to the interface are s_1 and s_2 , respectively. In the case of planar geometry, the dipole charge, q , has image charge q_n at distance s_1 in the nonpolar phase below the interface and the image charge, $-q_n$, of the opposite charge, $-q$, is at distance s_2 below the interface. Hence, the value of the electrostatic interaction energy between the dipole and the nonpolar phase, u_d^0 , is calculated using the simple expression:

$$\frac{u_d^0}{k_B T} = (1 - 2\alpha) z_c^2 \left[\frac{L_B}{2s_1} + \frac{L_B}{2s_2} - \frac{2L_B}{(d^2 + 4s_1s_2)^{1/2}} \right] \quad (\text{A6})$$

see Eq. (A5) and Fig. A2.

Appendix B. Spherical geometry

In the case of spherical geometry, the dividing surface between the dielectric phases is a sphere with radius R_s and center O (Fig. 2). The position of the charge can be outside the

sphere at distance R_s+s from the center (Fig. 2a) when the nonpolar phase is inside the sphere. In the opposite case, when the nonpolar phase is outside the sphere, the distance between the charge and the center O is R_s-s (Fig. 2b). The exact solutions of the electrostatic problems in spherical coordinates with radial distance r and polar angle θ are described in the literature [2]. Below, we summarize these solutions and apply them to calculate the respective expressions for the electrostatic interaction energies in the cases of charges and dipoles. The distance between the charge and an arbitrary point $A(r, \theta)$ is denoted by r_A . The general solutions are presented as series with respect to the Legendre polynomials, $P_n(\cos \theta)$, where $n = 0, 1, 2, \dots$, with coefficients depending on the radial coordinate, r .

B1. The nonpolar phase is inside the sphere

The general solution of the Laplace equation for the electrostatic potential inside the dielectric sphere, φ_n , can be presented in the following form [2]:

$$\varphi_n = \frac{q}{4\pi\epsilon_0\epsilon} \sum_{n=0}^{\infty} C_n r^n P_n(\cos \theta) \quad (\text{B1})$$

where C_n are unknown constants. The respective solution for the electrostatic potential outside this sphere, φ , is a superposition of the electrostatic potential of the charge resided in this phase and that induced from the nonpolar dielectric sphere:

$$\varphi = \frac{q}{4\pi\epsilon_0\epsilon} \left[\frac{1}{r_A} + \sum_{n=0}^{\infty} \frac{B_n}{r^{n+1}} P_n(\cos \theta) \right] \quad (\text{B2})$$

where B_n are unknown constants. The boundary conditions are defined at $r = R_s$, so that the inner expansion of $1/r_A$ in series:

$$\begin{aligned} \frac{1}{r_A} &= \frac{1}{[(R_s + s)^2 + r^2 - 2r(R_s + s)\cos \theta]^{1/2}} = \frac{1}{(R_s + s)(1 + t^2 - 2t\cos \theta)^{1/2}} \\ &= \frac{1}{R_s + s} \sum_{n=0}^{\infty} t^n P_n(\cos \theta) \quad \text{for } t = \frac{r}{R_s + s} < 1 \end{aligned} \quad (\text{B3})$$

should be used to apply the boundary conditions. Therefore, one represents Eq. (B2) in the following equivalent form:

$$\varphi = \frac{q}{4\pi\epsilon_0\epsilon} \left[\sum_{n=0}^{\infty} \frac{r^n}{(R_s + s)^{n+1}} P_n(\cos \theta) + \sum_{n=0}^{\infty} \frac{B_n}{r^{n+1}} P_n(\cos \theta) \right] \quad \text{for } r < R_s + s \quad (\text{B4})$$

The function for the electrostatic potential at the boundary is continuous and the surface charge density is equal to zero at $r = R_s$. Applying these boundary conditions to the general

solutions, Eqs. (B1) and (B4), one obtains the following linear system of equations for the unknown constants (B_n and C_n , $n = 0, 1, 2, \dots$) [2]:

$$\frac{R_s^n}{(R_s + s)^{n+1}} + \frac{B_n}{R_s^{n+1}} = C_n R_s^n, \quad \varepsilon \frac{n R_s^{n-1}}{(R_s + s)^{n+1}} - \varepsilon \frac{(n+1) B_n}{R_s^{n+2}} = \varepsilon_n n C_n R_s^{n-1} \quad (\text{B5})$$

The solution of this system of equations, Eq. (B5), is given by the expressions: i) for $n = 0$:

$$B_0 = 0, \quad C_0 = \frac{1}{R_s + s} \quad (\text{B6})$$

ii) for $n > 0$:

$$B_n = \frac{n}{n+1-\alpha} \frac{(1-2\alpha) R_s^{2n+1}}{(R_s + s)^{n+1}}, \quad C_n = \frac{1}{(R_s + s)^{n+1}} + \frac{B_n}{R_s^{2n+1}} \quad (\text{B7})$$

Therefore, the final exact solution of the considered electrostatic problem in the outer dielectric phase reads [2]:

$$\varphi = \frac{q}{4\pi\varepsilon_0\varepsilon R_s} \left[\frac{R_s}{r_A} + (1-2\alpha) S_{\text{out}} \left(\frac{s}{R_s}, \frac{r-R_s}{R_s}, \theta \right) \right] \quad \text{for } r \geq R_s \quad (\text{B8})$$

where function S_{out} is given by the following definition:

$$S_{\text{out}} \left(\frac{s}{R_s}, \frac{r-R_s}{R_s}, \theta \right) \equiv \sum_{n=1}^{\infty} \frac{n}{n+1-\alpha} \left(1 + \frac{s}{R_s} \right)^{-n-1} \left(1 + \frac{r-R_s}{R_s} \right)^{-n-1} P_n(\cos \theta) \quad (\text{B9})$$

The function, S_{out} , describes the induced electrostatic potential because of the nonpolar sphere.

The electrostatic interaction energy, u_c , between the charge and the nonpolar phase is equal to the charge, q , multiplied by the induced electrostatic potential at the charge position, $r = R_s + s$ and $\theta = 0$:

$$\frac{u_c}{k_B T} = (1-2\alpha) z_c^2 \frac{L_B}{R_s} S_{\text{out}} \left(\frac{s}{R_s}, \frac{s}{R_s}, 0 \right) \quad (\text{B10})$$

In the case of dipoles, the two dipole charges with the closest distances to the spherical surface s_1 and s_2 , the dipole length d , and the radius of sphere R_s define the polar angle, θ_d , between the radius vectors of the charge positions:

$$d^2 = (R_s + s_1)^2 + (R_s + s_2)^2 - 2(R_s + s_1)(R_s + s_2) \cos \theta_d \quad (\text{B11})$$

The electrostatic potential in the outer phase at an arbitrary point A is a superposition of the electrostatic potentials of charge q at distance r_A^+ from point A and that of charge $-q$ at distance r_A^- from point A . Thus from Eq. (B8), it follows that the exact solution of the electrostatic problem for an arbitrary dipole reads:

$$\varphi = \frac{q}{4\pi\epsilon_0\epsilon R_s} \left[\frac{R_s}{r_A^+} - \frac{R_s}{r_A^-} + (1-2\alpha)S_{\text{out}}\left(\frac{s_1}{R_s}, \frac{r-R_s}{R_s}, \theta\right) - (1-2\alpha)S_{\text{out}}\left(\frac{s_2}{R_s}, \frac{r-R_s}{R_s}, \theta-\theta_d\right) \right] \quad (\text{B12})$$

The electrostatic interaction energy, u_d , between the dipole and the nonpolar phase is equal to the sum of the charge, q , multiplied by the induced electrostatic potential at the charge position, $r = R_s + s_1$ and $\theta = 0$, and the opposite charge, $-q$, multiplied by the induced electrostatic potential at its position, $r = R_s + s_2$ and $\theta = \theta_d$:

$$\frac{u_d}{k_B T} = (1-2\alpha)z_c^2 \frac{L_B}{R_s} \left\{ S_{\text{out}}\left(\frac{s_1}{R_s}, \frac{s_1}{R_s}, 0\right) + S_{\text{out}}\left(\frac{s_2}{R_s}, \frac{s_2}{R_s}, 0\right) - 2S_{\text{out}}\left(\frac{s_1}{R_s}, \frac{s_2}{R_s}, \theta_d\right) \right\} \quad (\text{B13})$$

The derived analytical interpolations and the used procedures for precise calculations of u_c and u_d are discussed in Appendix B3.

B2. The nonpolar phase is outside the sphere

In this case, charge q is inside the sphere at position $r = R_s - s$ and $\theta = 0$ (Fig. 2b). The general solutions of the Laplace equation for the electrostatic potentials, φ_n and φ , are analogous to those given by Eqs. (B1) and (B2) [2]:

$$\varphi_n = \frac{q}{4\pi\epsilon_0\epsilon} \sum_{n=0}^{\infty} \frac{B_n}{r^{n+1}} P_n(\cos\theta) \quad (\text{B14})$$

$$\varphi = \frac{q}{4\pi\epsilon_0\epsilon} \left[\frac{1}{r_A} + \sum_{n=0}^{\infty} C_n r^n P_n(\cos\theta) \right] \quad (\text{B15})$$

where B_n and C_n are unknown constants. The boundary conditions are defined at $r = R_s$, so that the alternative outer expansion of $1/r_A$ in series:

$$\begin{aligned} \frac{1}{r_A} &= \frac{1}{[r^2 + (R_s - s)^2 - 2r(R_s - s)\cos\theta]^{1/2}} = \frac{1}{r(1+t^2 - 2t\cos\theta)^{1/2}} \\ &= \frac{1}{r} \sum_{n=0}^{\infty} t^n P_n(\cos\theta) \quad \text{for } t = \frac{R_s - s}{r} < 1 \end{aligned} \quad (\text{B16})$$

should be used. The substitution of this expansion into Eq. (B15) leads to the equivalent form of the solution for the electrostatic potential in the inner phase:

$$\varphi = \frac{q}{4\pi\epsilon_0\epsilon} \left[\sum_{n=0}^{\infty} \frac{(R_s - s)^n}{r^{n+1}} P_n(\cos\theta) + \sum_{n=0}^{\infty} C_n r^n P_n(\cos\theta) \right] \quad \text{for } r > R_s - s \quad (\text{B17})$$

Applying the boundary conditions at the dividing surface $r = R_s$ to the general solutions, Eqs. (B14) and (B17), one obtains the respective linear system of equations for the unknown constants (B_n and C_n , $n = 0, 1, 2, \dots$):

$$C_n R_s^n + \frac{(R_s - s)^n}{R_s^{n+1}} = \frac{B_n}{R_s^{n+1}}, \quad \varepsilon n C_n R_s^{n-1} - \varepsilon \frac{(n+1)(R_s - s)^n}{R_s^{n+2}} = -\varepsilon_n \frac{n+1}{R_s^{n+2}} B_n \quad (\text{B18})$$

The solution of this system of equations is: i) for $n = 0$:

$$B_0 = \frac{\varepsilon}{\varepsilon_n}, \quad C_0 = \frac{\varepsilon - \varepsilon_n}{\varepsilon_n} \frac{1}{R_s} \quad (\text{B19})$$

ii) for $n > 0$:

$$B_n = (R_s - s)^n + C_n R_s^{2n+1}, \quad C_n = (1 - 2\alpha) \frac{(n+1)(R_s - s)^n}{(n+\alpha)R_s^{2n+1}} \quad (\text{B20})$$

From Eqs. (B15), (B19) and (B20), one obtains the final exact solution of the considered electrostatic problem in the inner dielectric phase [2]:

$$\varphi = \frac{q}{4\pi\varepsilon_0\varepsilon R_s} \left[\frac{R_s}{r_A} + \frac{\varepsilon - \varepsilon_n}{\varepsilon_n} + (1 - 2\alpha) S_{\text{inn}} \left(\frac{s}{R_s}, \frac{R_s - r}{R_s}, \theta \right) \right] \quad \text{for } r \leq R_s \quad (\text{B21})$$

Here the definition of function S_{inn} is

$$S_{\text{inn}} \left(\frac{s}{R_s}, \frac{R_s - r}{R_s}, \theta \right) \equiv \sum_{n=1}^{\infty} \frac{n+1}{n+\alpha} \left(1 - \frac{s}{R_s}\right)^n \left(1 - \frac{R_s - r}{R_s}\right)^n P_n(\cos \theta) \quad (\text{B22})$$

Note that $S_{\text{inn}} = 0$ for $r = 0$ and hence, the induced electrostatic potential at the sphere center is different than zero, see the second term in the right-hand side of Eq. (B21).

The electrostatic interaction energy, u_c , between the charge and the nonpolar phase is equal to the charge multiplied by the induced electrostatic potential at the charge position, $r = R_s - s$ and $\theta = 0$, (see Appendix B1). Thus from Eq. (B21), we derive the following expression for the dimensionless value of u_c :

$$\frac{u_c}{k_B T} = z_c^2 \frac{L_B}{R_s} \left[\frac{\varepsilon - \varepsilon_n}{\varepsilon_n} + (1 - 2\alpha) S_{\text{inn}} \left(\frac{s}{R_s}, \frac{s}{R_s}, 0 \right) \right] \quad (\text{B23})$$

In the case of dipoles with the closest distances from the dipole charges to the spherical surface s_1 and s_2 , the dipole length d , the radius of sphere R_s , and the polar angle θ_d between the radius vectors of the charge positions, one uses the following relationship:

$$d^2 = (R_s - s_1)^2 + (R_s - s_2)^2 - 2(R_s - s_1)(R_s - s_2) \cos \theta_d \quad (\text{B24})$$

If the distances from given point A in the inner phase to the charges q and $-q$ are r_A^+ and r_A^- , respectively, then the superposition of the respective solutions given by Eq. (B21) yields:

$$\varphi = \frac{q}{4\pi\varepsilon_0\varepsilon R_s} \left[\frac{R_s}{r_A^+} - \frac{R_s}{r_A^-} + (1 - 2\alpha) S_{\text{inn}} \left(\frac{s_1}{R_s}, \frac{R_s - r}{R_s}, \theta \right) - (1 - 2\alpha) S_{\text{inn}} \left(\frac{s_2}{R_s}, \frac{R_s - r}{R_s}, \theta - \theta_d \right) \right] \quad (\text{B25})$$

Note, that the zero order term appearing in the right-hand side of Eq. (B21), $(\varepsilon - \varepsilon_n) / \varepsilon_n$, disappears in the solution for the electrostatic potential in the case of dipoles, Eq. (B25). Finally, the electrostatic interaction energy, u_d , between the dipole and the outer nonpolar phase is equal to the sum of the charges, q and $-q$, multiplied by the induced electrostatic potential at their positions:

$$\frac{u_d}{k_B T} = (1 - 2\alpha) z_c^2 \frac{L_B}{R_s} [S_{\text{inn}}(\frac{s_1}{R_s}, \frac{s_1}{R_s}, 0) + S_{\text{inn}}(\frac{s_2}{R_s}, \frac{s_2}{R_s}, 0) - 2S_{\text{inn}}(\frac{s_1}{R_s}, \frac{s_2}{R_s}, \theta_d)] \quad (\text{B26})$$

The respective analytical interpolations and the procedures for precise calculations of u_c and u_d are discussed in Appendix B3.

B3. Procedures for precise calculations of the electrostatic interaction energies

Charges and dipoles outside the sphere of nonpolar phase. If the charges and dipoles are outside the sphere, then the respective expressions for the interaction energies are given by Eqs. (B10) and (B13). The series converge slowly in their original form and it is difficult to obtain analytic interpolation expressions, which are convenient for fast calculations. One possible way for precise calculations is to use the identity

$$\frac{n}{n+1-\alpha} = 1 - \frac{1-\alpha}{n+1} - \frac{\alpha(1-\alpha)}{(n+1)(n+1-\alpha)} \quad (\text{B27})$$

The last term in the right-hand side of Eq. (B27) is considerably smaller than unity, because of $\alpha(1-\alpha) \leq 1/4$ and $(n+1)(n+1-\alpha) > n(n+1)$. Thus, one represents the general function, $\Phi_{\text{out}}(t, \theta)$, appearing in the right-hand sides of Eqs. (B10) and (B13), in the following equivalent form:

$$\begin{aligned} \Phi_{\text{out}}(t, \theta) = & t \sum_{n=1}^{\infty} t^n P_n(\cos \theta) - (1-\alpha) \sum_{n=1}^{\infty} \frac{t^{n+1}}{n+1} P_n(\cos \theta) \\ & - \alpha(1-\alpha) \sum_{n=1}^{\infty} \frac{t^{n+1} P_n(\cos \theta)}{(n+1)(n+1-\alpha)} \quad \text{for } 0 < t < 1 \end{aligned} \quad (\text{B28})$$

see Eqs. (B9) and (B27). Note that the last sum in the right-hand side of Eq. (B28) converges fast and it is easy to calculate this sum numerically with an excellent precision.

The first two sums in the right-hand side of Eq. (B28) can be calculated analytically. Indeed, the first sum corresponds to the generating function of the Legendre polynomials:

$$\sum_{n=1}^{\infty} t^n P_n(\cos \theta) = \frac{1}{(1+t^2 - 2t \cos \theta)^{1/2}} - 1 \quad (\text{B29})$$

The integration of Eq. (B29) with respect to t leads to the second sum appearing in the right-hand side of Eq. (B28):

$$\begin{aligned} \sum_{n=1}^{\infty} \frac{t^{n+1}}{n+1} P_n(\cos \theta) &= \int_0^t \left[\frac{1}{(1+\tau^2 - 2\tau \cos \theta)^{1/2}} - 1 \right] d\tau \\ &= -\ln \left[\frac{(1+t^2 - 2t \cos \theta)^{1/2} + \cos \theta - t}{1 + \cos \theta} \right] - t \end{aligned} \quad (\text{B30})$$

Therefore, the final interpolation formula for the calculation of $\Phi_{\text{out}}(t, \theta)$, valid for all physical values of $0 < \alpha < 1$ and $0 < t < 1$, reads:

$$\Phi_{\text{out}}(t, \theta) \approx \frac{t}{(1+t^2 - 2t \cos \theta)^{1/2}} - \alpha t + (1-\alpha) \ln \left[\frac{(1+t^2 - 2t \cos \theta)^{1/2} + \cos \theta - t}{1 + \cos \theta} \right] \quad (\text{B31})$$

Note that

$$S_{\text{out}}\left(\frac{s}{R_s}, \frac{s}{R_s}, 0\right) = \Phi_{\text{out}}\left[\left(\frac{R_s}{R_s + s}\right)^2, 0\right] \quad \text{and} \quad S_{\text{out}}\left(\frac{s_1}{R_s}, \frac{s_2}{R_s}, \theta_d\right) = \Phi_{\text{out}}\left[\frac{R_s^2}{(R_s + s_1)(R_s + s_2)}, \theta_d\right]$$

Fig. B1 shows the calculated relative error of the interpolation formula for $\Phi_{\text{out}}(t, 0)$, see Eq. (B31), for several typical values of α . As should be, the maximum relative error is obtained for $\alpha = 0.5$ and the relative error decreases with the increase of $|2\alpha - 1|$. The parameter $\alpha = 0.5$ when the dielectric constants of the phases are equal, i.e. $\varepsilon = \varepsilon_n$ and there is no interfacial boundary. If $\varepsilon > \varepsilon_n$ then $\alpha < 0.5$, e.g. for typical values of water and hydrocarbon $\varepsilon = 78$ and $\varepsilon_n = 2$, respectively, which results in $\alpha = 1/40$. For ethanol-water mixtures with high alcohol content and elevated temperature the dielectric constant could decrease to e.g. $\varepsilon = 18$, then for $\varepsilon_n = 2$, $\alpha = 1/10$. For the hypothetical case of $\varepsilon < \varepsilon_n$ and $\alpha > 0.5$, for example $\varepsilon = 5$ and $\varepsilon_n = 45$, which results in $\alpha = 9/10$.

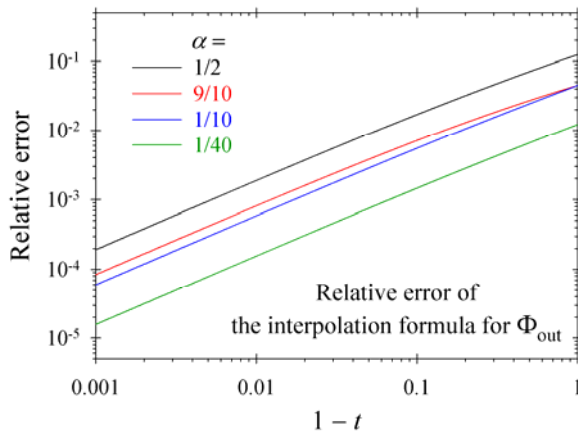


Fig. B1. Relative error of the interpolation formula for $\Phi_{\text{out}}(t, 0)$.

When the distance between the charges and dipoles to the dividing surface decreases, then the value of parameter t increases to unity and the relative error decreases considerably. In the typical cases of dipoles, the polar angles, θ_d , are small, see Eq. (B11), and the precision of the interpolation formula is close to that illustrated for $\Phi_{\text{out}}(t, 0)$ in Fig. B1.

To account for the curvature effect (radius of the sphere) on the electrostatic interaction energy between the individual charge and the nonpolar sphere, Eq. (B10) is presented in its equivalent form:

$$\frac{u_c - u_c^0}{k_B T} = \frac{L_B z_c^2}{2s} F_{\text{out}}, \quad F_{\text{out}} \equiv (1 - 2\alpha) \left\{ \frac{2s}{R_s} \Phi_{\text{out}} \left[\frac{R_s^2}{(R_s + s)^2}, 0 \right] - 1 \right\} \quad (\text{B32})$$

The difference between the interaction energies, $u_c - u_c^0$, accounts for the curvature effect of the sphere. In fact, for a fixed value of s , this difference depends on the sphere radius through the ratio s/R_s and the parameter α , i.e. on the ratio between the dielectric constants, see Eq. (B32).

Fig. B2 illustrates the dependence of F_{out} on α and s/R_s . Note that $(\varepsilon - \varepsilon_n)/(\varepsilon + \varepsilon_n) = 1 - 2\alpha$ and the sign of $u_c - u_c^0$ changes from negative for $\alpha < 1/2$ to positive for $\alpha > 1/2$, see Eq. (B32). With the increase of the sphere radius (i.e. decrease of s/R_s), the differences between the interaction energies decrease. In the opposite case, i.e. R_s decreases (increase of s/R_s) the magnitude of interaction energy difference significantly increases (Fig. B2). Note that the Bjerrum length, L_B , for water at 25 °C is 7.1 Å and even for $s = 3.5$ Å and $z_c^2 = 1$, the scaling factor in Eq. (B32) is equal to 1, which gives the interaction energy difference of $k_B T$ multiplied by the respective value of F_{out} .

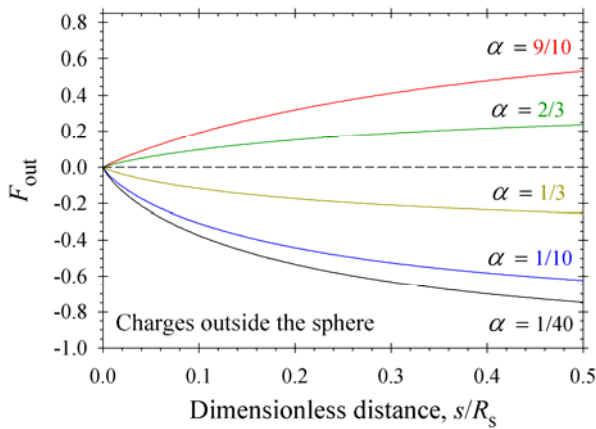


Fig. B2. Effect of sphere radius R_s (R_s decrease leads to s/R_s increase) on the electrostatic interaction energy between the charge in the outer dielectric phase and the nonpolar phase in the sphere.

In the case of dipoles in the outer dielectric phase, the electrostatic interaction difference, $f_{\text{dip}} = u_d - u_d^0$, is convenient to be presented in the following form:

$$\frac{f_{\text{dip}}}{k_{\text{B}}T} = \frac{u_{\text{d}} - u_{\text{d}}^0}{k_{\text{B}}T} = z_{\text{c}}^2 \left[\frac{L_{\text{B}}}{2s_1} + \frac{L_{\text{B}}}{2s_2} - \frac{2L_{\text{B}}}{(d^2 + 4s_1s_2)^{1/2}} \right] D_{\text{out}} \quad (\text{B33a})$$

where function D_{out} accounts for the curvature effect of the spherical nonpolar phase. From Eqs. (A6) and (B13), the exact expression for D_{out} reads:

$$D_{\text{out}} = \frac{2(1-2\alpha)s_1s_2(d^2 + 4s_1s_2)^{1/2}}{R_{\text{s}}[(s_1 + s_2)(d^2 + 4s_1s_2)^{1/2} - 4s_1s_2]} \left\{ \Phi_{\text{out}}\left[\left(\frac{R_{\text{s}}}{R_{\text{s}} + s_1}\right)^2, 0\right] + \Phi_{\text{out}}\left[\left(\frac{R_{\text{s}}}{R_{\text{s}} + s_2}\right)^2, 0\right] \right. \\ \left. - 2\Phi_{\text{out}}\left[\frac{R_{\text{s}}^2}{(R_{\text{s}} + s_1)(R_{\text{s}} + s_2)}, \theta_{\text{d}}\right] \right\} - (1-2\alpha) \quad (\text{B33b})$$

The dependencies of the calculated values of D_{out} on the system parameters are shown in Fig. 4 and discussed in the main text.

Charges and dipoles inside the dielectric sphere. In this case, the expressions for the interaction energies are given by Eqs. (B23) and (B26). Again the series converge slowly in their original form. For that reason, one considers the following identity:

$$\frac{n+1}{n+\alpha} = 1 + \frac{1-\alpha}{n} - \frac{\alpha(1-\alpha)}{n(n+\alpha)} \quad (\text{B34})$$

where the last term is considerably smaller than unity. Therefore, one represents the general function, $\Phi_{\text{inn}}(t, \theta)$, appearing in the right-hand sides of Eqs. (B23) and (B26), in the following equivalent form:

$$\Phi_{\text{inn}}(t, \theta) = \sum_{n=1}^{\infty} t^n P_n(\cos \theta) + (1-\alpha) \sum_{n=1}^{\infty} \frac{t^n}{n} P_n(\cos \theta) \\ - \alpha(1-\alpha) \sum_{n=1}^{\infty} \frac{t^n P_n(\cos \theta)}{n(n+\alpha)} \quad \text{for } 0 < t < 1 \quad (\text{B35})$$

The last sum in the right-hand side of Eq. (B35) converges fast and it is easy to calculate this sum with a high precision.

The first sum in the right-hand side of Eq. (B35) is given by the exact formula, Eq. (B29). The exact result for the second sum is calculated as follows:

$$\sum_{n=1}^{\infty} \frac{t^n}{n} P_n(\cos \theta) = \int_0^t \left[\frac{1}{\tau(1+\tau^2 - 2\tau \cos \theta)^{1/2}} - \frac{1}{\tau} \right] d\tau \\ = -\ln \left[\frac{(1+t^2 - 2t \cos \theta)^{1/2} + 1 - t \cos \theta}{2} \right] \quad (\text{B36})$$

Therefore, the final interpolation formula for the calculation of $\Phi_{\text{inn}}(t, \theta)$, valid for all physical values of $0 < \alpha < 1$ and $0 < t < 1$, reads:

$$\Phi_{\text{inn}}(t, \theta) \approx \frac{1}{(1+t^2-2t\cos\theta)^{1/2}} - 1 - (1-\alpha) \ln\left[\frac{(1+t^2-2t\cos\theta)^{1/2} + 1 - t\cos\theta}{2}\right] \quad (\text{B37})$$

Fig. B3 shows the calculated relative error of the interpolation formula for $\Phi_{\text{inn}}(t, 0)$, see Eq. (B37) for typical ratios between the dielectric constants as discussed above. Again the maximum relative error is obtained for $\alpha = 0.5$. The relative error decreases considerably with: the increase of $|2\alpha-1|$; the increase of parameter t (for charges and dipoles closer to the dividing surface); the increase of polar angle θ_d .

Note that

$$S_{\text{inn}}\left(\frac{s}{R_s}, \frac{s}{R_s}, 0\right) = \Phi_{\text{inn}}\left[\frac{(R_s - s)^2}{R_s^2}, 0\right] \quad \text{and} \quad S_{\text{inn}}\left(\frac{s_1}{R_s}, \frac{s_2}{R_s}, \theta_d\right) = \Phi_{\text{inn}}\left[\frac{(R_s - s_1)(R_s - s_2)}{R_s^2}, \theta_d\right]$$

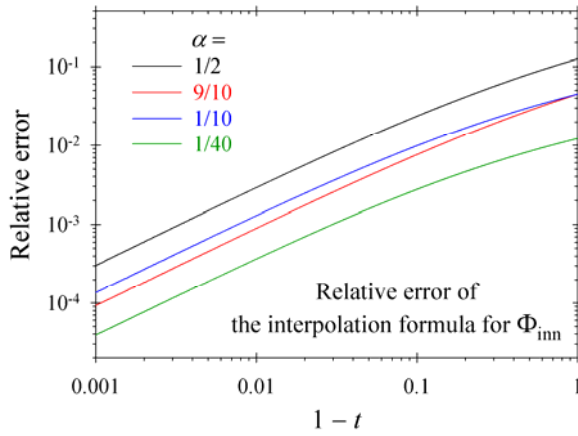


Fig. B3. Relative error of the interpolation formula for $\Phi_{\text{inn}}(t, 0)$ for several characteristic values of α .

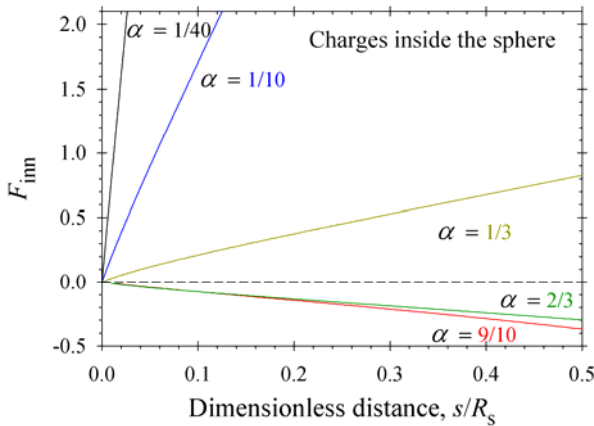


Fig. B4. Effect of sphere radius R_s on the electrostatic interaction energy between the charge in the inner phase (sphere) and the nonpolar phase outside the sphere.

The difference between the interaction energies, $u_c - u_c^0$, accounts for the curvature effect of the sphere. For a fixed value of s , this difference is described by the function F_{inn} , given by the following definition:

$$\frac{u_c - u_c^0}{k_B T} = \frac{L_B z_c^2}{2s} F_{\text{inn}}, \quad F_{\text{inn}} \equiv (1 - 2\alpha) \left\{ \frac{2s}{\alpha R_s} + \frac{2s}{R_s} \Phi_{\text{inn}} \left[\frac{(R_s - s)^2}{R_s^2}, 0 \right] - 1 \right\} \quad (\text{B38})$$

see Eq. (B23).

If the charge is in the inner phase (sphere), then the energy difference for a fixed distance s is characterized by the function F_{inn} , see Eq. (B38). The curvature effect on the electrostatic energy difference is illustrated in Fig. B4. Note that the solution for the electrostatic potential, Eq. (B21), contains non-zero value of the induced potential at center O , i.e. for $r = 0$, which increases considerably for the decrease of the dielectric constant of the outer phase, ε_n . Hence this leads to a steep increase of F_{inn} for small values of α . As it should be expected, the signs of $u_c - u_c^0$ are opposite to those in Fig. B2 – they are positive for $\alpha < 1/2$ ($\varepsilon_n < \varepsilon$) and negative for $\alpha > 1/2$ ($\varepsilon_n > \varepsilon$). Note that the electrostatic interactions are much stronger when the dielectric constant of the outer nonpolar phase is lower than that of the inner dielectric phase.

In the case of dipoles resided in the inner dielectric phase, the electrostatic interaction difference, $u_d - u_d^0$, is presented in the analogous form to Eq. (B33a):

$$\frac{f_{\text{dip}}}{k_B T} = \frac{u_d - u_d^0}{k_B T} = z_c^2 \left[\frac{L_B}{2s_1} + \frac{L_B}{2s_2} - \frac{2L_B}{(d^2 + 4s_1 s_2)^{1/2}} \right] D_{\text{inn}} \quad (\text{B39a})$$

where function D_{inn} accounts for the curvature effect of outer nonpolar phase. From Eqs. (A6) and (B26), the exact expression for D_{inn} reads:

$$D_{\text{inn}} = \frac{2(1 - 2\alpha)s_1 s_2 (d^2 + 4s_1 s_2)^{1/2}}{R_s [(s_1 + s_2)(d^2 + 4s_1 s_2)^{1/2} - 4s_1 s_2]} \left\{ \Phi_{\text{inn}} \left[\left(\frac{R_s - s_1}{R_s} \right)^2, 0 \right] + \Phi_{\text{inn}} \left[\left(\frac{R_s - s_2}{R_s} \right)^2, 0 \right] \right. \\ \left. - 2\Phi_{\text{inn}} \left[\frac{(R_s - s_1)(R_s - s_2)}{R_s^2}, \theta_d \right] \right\} - (1 - 2\alpha) \quad (\text{B39b})$$

The dependencies of the calculated values of D_{inn} on the system parameters are shown in Fig. 5 and discussed in the main text.

Appendix C. Cylindrical geometry

In the case of cylindrical geometry, the dividing surface between the dielectric phases is a cylinder with radius R_c . We define cylindrical coordinate system $O\rho\phi z$, where Oz is the axis of revolution and ρ and ϕ are the radial and polar coordinates, respectively (Fig. 3). The position of the charge can be outside the cylinder with charge coordinates $\rho = R_c + s$, $\phi = 0$, and $z = 0$ (Fig. 3a), when the nonpolar phase is inside the cylinder. In the opposite case (the dielectric phase is inside the cylinder), the charge coordinates are $\rho = R_c - s$, $\phi = 0$, and $z = 0$

(Fig. 3b). The exact solutions of the respective electrostatic problems are reported in the literature [3]. The problem in Appendix B is 2D because of the symmetry (Fig. 2), while in the case of cylinder, the electrostatic problem is essentially 3D (Fig. 3).

C1. The nonpolar phase is inside the cylinder

The general solution of the electrostatic problem in the inner nonpolar phase ($\rho < R_c$) is presented as follows [3]:

$$\begin{aligned} \varphi_n = & \frac{q}{4\pi\epsilon_0\epsilon R_c} \left[\frac{2}{\pi} \int_0^\infty C_0(k) I_0\left(k \frac{\rho}{R_c}\right) \cos\left(k \frac{z}{R_c}\right) dk \right. \\ & \left. + \sum_{n=1}^\infty \frac{4}{\pi} \int_0^\infty C_n(k) I_n\left(k \frac{\rho}{R_c}\right) \cos(n\phi) \cos\left(k \frac{z}{R_c}\right) dk \right] \end{aligned} \quad (C1)$$

where $C_n(k)$ are unknown functions and I_n are the modified Bessel functions of the first kind ($n = 0, 1, \dots$). The respective general solution for the electrostatic potential outside the cylinder ($\rho > R_c$) is given by the relationship [3]:

$$\begin{aligned} \varphi = & \frac{q}{4\pi\epsilon_0\epsilon R_c} \left[\frac{R_c}{r_A} + \frac{\epsilon - \epsilon_n}{\epsilon + \epsilon_n} \frac{2}{\pi} \int_0^\infty B_0(k) K_0\left(k \frac{\rho}{R_c}\right) \cos\left(k \frac{z}{R_c}\right) dk \right. \\ & \left. + \frac{\epsilon - \epsilon_n}{\epsilon + \epsilon_n} \sum_{n=1}^\infty \frac{4}{\pi} \int_0^\infty B_n(k) K_n\left(k \frac{\rho}{R_c}\right) \cos(n\phi) \cos\left(k \frac{z}{R_c}\right) dk \right] \end{aligned} \quad (C2)$$

Here: $B_n(k)$ are unknown functions; K_n are the modified Bessel functions of the second kind ($n = 0, 1, \dots$); r_A is the distance from the charge to an arbitrary point $A(\rho, \phi, z)$, see Fig. 3a.

The boundary conditions are applied at the cylindrical dividing surface, $\rho = R_c$, which corresponds to the inner integral representation of $1/r_A$:

$$\begin{aligned} \frac{R_c}{r_A} = & \frac{2}{\pi} \int_0^\infty I_0\left(k \frac{\rho}{R_c}\right) K_0\left[k\left(1 + \frac{s}{R_c}\right)\right] \cos\left(k \frac{z}{R_c}\right) dk \\ & + \frac{4}{\pi} \sum_{n=1}^\infty \int_0^\infty I_n\left(k \frac{\rho}{R_c}\right) K_n\left[k\left(1 + \frac{s}{R_c}\right)\right] \cos(n\phi) \cos\left(k \frac{z}{R_c}\right) dk \quad \text{for } \rho < R_c + s \end{aligned} \quad (C3)$$

The unknown functions are determined from the following system of equations: i) the electrostatic potential is a continuous function at the cylindrical surface:

$$K_n\left[k\left(1 + \frac{s}{R_c}\right)\right] + \frac{\epsilon - \epsilon_n}{\epsilon + \epsilon_n} \frac{K_n(k)}{I_n(k)} B_n(k) - C_n(k) = 0 \quad (n = 0, 1, 2, \dots) \quad (C4)$$

ii) the surface charge density at the dividing surface is equal to zero:

$$\varepsilon \frac{\partial \varphi}{\partial \rho} \Big|_{\rho=R_c} = \varepsilon_n \frac{\partial \varphi_n}{\partial \rho} \Big|_{\rho=R_c} \quad (\text{C5})$$

The substitution of the obtained expressions, Eqs. (C1)–(C3), into the boundary condition, Eq. (C5), yields:

$$K_0 \left[k \left(1 + \frac{s}{R_c} \right) \right] - (1 - 2\alpha) \frac{K_1(k)}{I_1(k)} B_0(k) - \frac{\varepsilon_n}{\varepsilon} C_0(k) = 0 \quad (\text{C6})$$

$$K_n \left[k \left(1 + \frac{s}{R_c} \right) \right] - (1 - 2\alpha) \frac{K_{n+1}(k) + K_{n-1}(k)}{I_{n+1}(k) + I_{n-1}(k)} B_n(k) - \frac{\varepsilon_n}{\varepsilon} C_n(k) = 0 \quad (n > 0) \quad (\text{C7})$$

The exact solution of the linear system of equations, Eqs. (C4), (C6), and (C7), for coefficients $B_n(k)$ ($n = 0, 1, \dots$) reads:

$$B_0(k) = \frac{I_1(k) K_0 \left[k \left(1 + \frac{s}{R_c} \right) \right]}{K_1(k) [1 - \alpha b_0(k)]} \quad (\text{C8})$$

$$B_n(k) = \frac{[I_{n+1}(k) + I_{n-1}(k)] K_n \left[k \left(1 + \frac{s}{R_c} \right) \right]}{[K_{n+1}(k) + K_{n-1}(k)] [1 - \alpha b_n(k)]} \quad (n > 0) \quad (\text{C9})$$

where functions $b_0(k), b_1(k), \dots$ are given by the definitions:

$$b_0(k) \equiv 1 - \frac{I_1(k) K_0(k)}{I_0(k) K_1(k)} \quad (\text{C10})$$

$$b_n(k) \equiv 1 - \frac{K_n(k)}{I_n(k)} \frac{I_{n+1}(k) + I_{n-1}(k)}{K_{n+1}(k) + K_{n-1}(k)} \quad (n > 0) \quad (\text{C11})$$

From the obtained expressions for the coefficients, Eqs. (C8)–(C11), the final solution for the electrostatic potential, φ , in the outer dielectric phase, given by Eq. (C2), is presented in the following explicit form:

$$\varphi = \frac{q}{4\pi\varepsilon_0\varepsilon R_c} \left[\frac{R_c}{r_A} + (1 - 2\alpha) C_{\text{out}} \left(\frac{s}{R_c}, \frac{\rho - R_c}{R_c}, \phi, z \right) \right] \quad (\text{C12})$$

Here the induced electrostatic potential from the inner cylindrical phase is accounted for by the function C_{out} , which for cylinders is given by the following definition:

$$C_{\text{out}}(t_1, t_2, \phi, z) \equiv \frac{2}{\pi} \int_0^\infty \frac{I_1(k) K_0[k(1+t_1)] K_0[k(1+t_2)]}{K_1(k) [1 - \alpha b_0(k)]} \cos(k \frac{z}{R_c}) dk + \frac{4}{\pi} \sum_{n=1}^\infty \int_0^\infty \frac{[I_{n+1}(k) + I_{n-1}(k)] K_n[k(1+t_1)] K_n[k(1+t_2)]}{[K_{n+1}(k) + K_{n-1}(k)] [1 - \alpha b_n(k)]} \cos(n\phi) \cos(k \frac{z}{R_c}) dk \quad (\text{C13})$$

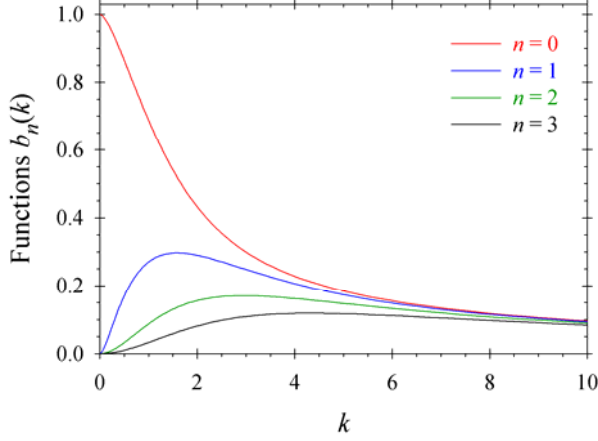


Fig. C1. Dependence of functions $b_n(k)$ on n and k , calculated after Eqs. (C10) and (C11).

The dependencies of functions $b_n(k)$ on n and k are shown in Fig. C1. One sees that $0 < b_n(k) \leq 1$ and $b_n(k)$ decrease with the increase both of n and k . Therefore, the terms $1 - \alpha \leq 1 - \alpha b_n(k) < 1$ in the integrands in the right-hand side of Eq. (C13) do not affect the convergence of the integrals.

The electrostatic interaction energy, u_c , between the charge and the nonpolar phase is equal to the charge, q , multiplied by the induced electrostatic potential at the charge position, $\rho = R_c + s$, $\phi = 0$, and $z = 0$ (Fig. 3a). Thus from Eq. (C12), we derive the following formula:

$$\frac{u_c}{k_B T} = (1 - 2\alpha) z_c^2 \frac{L_B}{R_c} C_{\text{out}}\left(\frac{s}{R_c}, \frac{s}{R_c}, 0, 0\right) \quad (\text{C14})$$

In the case of dipoles with dipole length d and closest distances s_1 and s_2 from the dipole charges to the dividing surface, the coordinates of charge q are $\rho = R_c + s_1$, $\phi = 0$, $z = 0$ and those of charge $-q$ are $\rho = R_c + s_2$, $\phi = \phi_d$, $z = z_d$. Hence, the dipole length, d , is calculated from the relationship:

$$d^2 = (R_c + s_1)^2 + (R_c + s_2)^2 - 2(R_c + s_1)(R_c + s_2) \cos \phi_d + z_d^2 \quad (\text{C15})$$

The electrostatic potential at an arbitrary point A in the outer dielectric phase is a superposition of the electrostatic potentials of charge q and opposite charge $-q$ at distances r_A^+ and r_A^- from point A , respectively. It follows from Eq. (C12) that the exact solution of the electrostatic problem in the case of dipoles reads:

$$\begin{aligned} \varphi = \frac{q}{4\pi\epsilon_0\epsilon R_c} \left[\frac{R_c}{r_A^+} - \frac{R_c}{r_A^-} + (1 - 2\alpha) C_{\text{out}}\left(\frac{s_1}{R_c}, \frac{\rho - R_c}{R_c}, \phi, z\right) - \right. \\ \left. - (1 - 2\alpha) C_{\text{out}}\left(\frac{s_2}{R_c}, \frac{\rho - R_c}{R_c}, \phi - \phi_d, z - z_d\right) \right] \quad (\text{C16}) \end{aligned}$$

The electrostatic interaction energy, u_d , between the dipole and the nonpolar phase is equal to the sum of the dipole charges, q and $-q$, multiplied by the induced electrostatic potential at their positions, so that:

$$\frac{u_d}{k_B T} = (1 - 2\alpha) z_c^2 \frac{L_B}{R_c} [C_{\text{out}}(\frac{s_1}{R_c}, \frac{s_1}{R_c}, 0, 0) + C_{\text{out}}(\frac{s_2}{R_c}, \frac{s_2}{R_c}, 0, 0) - 2C_{\text{out}}(\frac{s_1}{R_c}, \frac{s_2}{R_c}, \phi_d, z_d)] \quad (\text{C17})$$

see Eq. (C16). The procedures for precise calculations of u_c and u_d are discussed in Appendix C3.

C2. Charges and dipoles inside the dielectric cylinder

For charges in the inner dielectric phase, the general solution of the electrostatic problem in this phase ($\rho < R_c$) is presented as follows [3]:

$$\begin{aligned} \varphi = \frac{q}{4\pi\epsilon_0\epsilon R_c} & \left[\frac{R_c}{r_A} + \frac{\epsilon - \epsilon_n}{\epsilon + \epsilon_n} \frac{2}{\pi} \int_0^\infty C_0(k) I_0(k \frac{\rho}{R_c}) \cos(k \frac{z}{R_c}) dk \right. \\ & \left. + \frac{\epsilon - \epsilon_n}{\epsilon + \epsilon_n} \sum_{n=1}^\infty \frac{4}{\pi} \int_0^\infty C_n(k) I_n(k \frac{\rho}{R_c}) \cos(n\phi) \cos(k \frac{z}{R_c}) dk \right] \end{aligned} \quad (\text{C18})$$

where $C_n(k)$ are unknown functions ($n = 0, 1, \dots$) and r_A is the distance from the charge to an arbitrary point $A(\rho, \phi, z)$, see Fig. 3b. The respective general solution for the electrostatic potential outside the cylinder ($\rho > R_c$) reads [3]:

$$\begin{aligned} \varphi_n = \frac{q}{4\pi\epsilon_0\epsilon R_c} & \left[\frac{2}{\pi} \int_0^\infty B_0(k) K_0(k \frac{\rho}{R_c}) \cos(k \frac{z}{R_c}) dk \right. \\ & \left. + \sum_{n=1}^\infty \frac{4}{\pi} \int_0^\infty B_n(k) K_n(k \frac{\rho}{R_c}) \cos(n\phi) \cos(k \frac{z}{R_c}) dk \right] \end{aligned} \quad (\text{C19})$$

where $B_n(k)$ are unknown functions ($n = 0, 1, \dots$).

The boundary conditions are applied at the cylindrical dividing surface, $\rho = R_c$, which corresponds to the outer integral representation of $1/r_A$ (see Fig. 3b):

$$\begin{aligned} \frac{R_c}{r_A} = \frac{2}{\pi} \int_0^\infty & I_0[k(1 - \frac{s}{R_c})] K_0(k \frac{\rho}{R_c}) \cos(k \frac{z}{R_c}) dk \\ & + \frac{4}{\pi} \sum_{n=1}^\infty \int_0^\infty I_n[k(1 - \frac{s}{R_c})] K_n(k \frac{\rho}{R_c}) \cos(n\phi) \cos(k \frac{z}{R_c}) dk \quad \text{for } \rho > R_c - s \end{aligned} \quad (\text{C20})$$

The unknown functions are determined from the following system of equations: i) the electrostatic potential is a continuous function at the cylindrical surface:

$$I_n[k(1-\frac{s}{R_c})] + \frac{\varepsilon - \varepsilon_n}{\varepsilon + \varepsilon_n} \frac{I_n(k)}{K_n(k)} C_n(k) - B_n(k) = 0 \quad (n = 0, 1, 2, \dots) \quad (C21)$$

ii) the surface charge density at that surface is equal to zero and the substitution of the obtained expressions, Eqs. (C18)–(C20), into the boundary condition, Eq. (C5), yields:

$$I_0[k(1-\frac{s}{R_c})] - \frac{\varepsilon - \varepsilon_n}{\varepsilon + \varepsilon_n} \frac{I_1(k)}{K_1(k)} C_0(k) - \frac{\varepsilon_n}{\varepsilon} B_0(k) = 0 \quad (C22)$$

$$I_n[k(1-\frac{s}{R_c})] - \frac{\varepsilon - \varepsilon_n}{\varepsilon + \varepsilon_n} \frac{I_{n+1}(k) + I_{n-1}(k)}{K_{n+1}(k) + K_{n-1}(k)} C_n(k) - \frac{\varepsilon_n}{\varepsilon} B_n(k) = 0 \quad (n > 0) \quad (C23)$$

The solution of this system of equations for coefficients $C_n(k)$ ($n = 0, 1, \dots$) is presented as follows:

$$C_n(k) = \frac{K_n(k) I_n[k(1-\frac{s}{R_c})]}{I_n(k) [1 - (1-\alpha)b_n(k)]} \quad (n = 0, 1, \dots) \quad (C24)$$

Finally, from the obtained expression for the coefficients, Eq. (C24), the explicit form of the solution for the electrostatic problem for potential φ in the inner dielectric phase, given by Eq. (C18), is derived:

$$\varphi = \frac{q}{4\pi\varepsilon_0\varepsilon R_c} \left[\frac{R_c}{r_A} + (1-2\alpha) C_{\text{inn}} \left(\frac{s}{R_c}, \frac{R_c - \rho}{R_c}, \phi, z \right) \right] \quad (C25)$$

In this case, the induced electrostatic potential from the outer cylindrical phase is accounted for by function C_{inn} , which for cylinders is defined as follows:

$$C_{\text{inn}}(t_1, t_2, \phi, z) \equiv \frac{2}{\pi} \int_0^\infty \frac{K_0(k) I_0[k(1-t_1)] I_0[k(1-t_2)]}{I_0(k) [1 - (1-\alpha)b_0(k)]} \cos(k \frac{z}{R_c}) dk + \frac{4}{\pi} \sum_{n=1}^\infty \int_0^\infty \frac{K_n(k) I_n[k(1-t_1)] I_n[k(1-t_2)]}{I_n(k) [1 - (1-\alpha)b_n(k)]} \cos(n\phi) \cos(k \frac{z}{R_c}) dk \quad (C26)$$

The terms $\alpha \leq 1 - (1-\alpha)b_n(k) < 1$ in the integrands in the right-hand side of Eq. (C26) again do not affect the convergence of the integrals, see Fig. C1.

The electrostatic interaction energy, u_c , between the charge and the nonpolar phase is equal to the charge, q , multiplied by the induced electrostatic potential at the charge position, $\rho = R_c - s$, $\phi = 0$, and $z = 0$ (Fig. 3b). Using Eqs. (C25) and (C26) one obtains:

$$\frac{u_c}{k_B T} = (1-2\alpha) z_c^2 \frac{L_B}{R_c} C_{\text{inn}} \left(\frac{s}{R_c}, \frac{s}{R_c}, 0, 0 \right) \quad (C27)$$

Analogously to Appendix C1, in the case of dipoles with coordinates of charge q , $\rho = R_c - s_1$, $\phi = 0$, $z = 0$, and those of charge $-q$, $\rho = R_c - s_2$, $\phi = \phi_d$, $z = z_d$: i) the dipole length, d , is calculated from the expression:

$$d^2 = (R_c - s_1)^2 + (R_c - s_2)^2 - 2(R_c - s_1)(R_c - s_2) \cos \phi_d + z_d^2 \quad (\text{C28})$$

ii) the solution for the electrostatic potential in the inner phase reads

$$\begin{aligned} \varphi = \frac{q}{4\pi\epsilon_0\epsilon R_c} \left[\frac{R_c}{r_A^+} - \frac{R_c}{r_A^-} + (1-2\alpha)C_{\text{inn}}\left(\frac{s_1}{R_c}, \frac{R_c-\rho}{R_c}, \phi, z\right) - \right. \\ \left. -(1-2\alpha)C_{\text{inn}}\left(\frac{s_2}{R_c}, \frac{R_c-\rho}{R_c}, \phi-\phi_d, z-z_d\right) \right] \end{aligned} \quad (\text{C29})$$

Therefore, the respective electrostatic interaction energy, u_d , between the dipole and the nonpolar outer phase, which is equal to the sum of the charges, q and $-q$, multiplied by the induced electrostatic potential at their positions, is calculated from the following formula:

$$\frac{u_d}{k_B T} = (1-2\alpha)z_c^2 \frac{L_B}{R_c} \left[C_{\text{inn}}\left(\frac{s_1}{R_c}, \frac{s_1}{R_c}, 0, 0\right) + C_{\text{inn}}\left(\frac{s_2}{R_c}, \frac{s_2}{R_c}, 0, 0\right) - 2C_{\text{inn}}\left(\frac{s_1}{R_c}, \frac{s_2}{R_c}, \phi_d, z_d\right) \right] \quad (\text{C30})$$

The procedures for precise calculations of u_c and u_d are discussed in Appendix C3.

C3. Procedures for precise calculations of the electrostatic interaction energies

Charges and dipoles outside the dielectric cylinder. If the charges and dipoles are outside the cylinder, then the charge interaction energy is calculated from Eq. (C14). For large radii ($s/R_c \ll 1$), the asymptotic value of $C_{\text{out}}(s/R_c, s/R_c, 0, 0)$ is equal to $R_c/(2s)$. For numerical calculations, it is convenient to exclude this singularity using Eq. (C3).

To account for the curvature effect (radius R_c) on the interaction energy between the charge and the cylindrical nonpolar phase, Eq. (C14) is presented in its equivalent form:

$$\frac{u_c - u_c^0}{k_B T} = \frac{L_B z_c^2}{2s} F_{\text{out}}, \quad F_{\text{out}} \equiv (1-2\alpha) \left[\frac{2s}{R_c} C_{\text{out}}\left(\frac{s}{R_c}, \frac{s}{R_c}, 0, 0\right) - 1 \right] \quad (\text{C31})$$

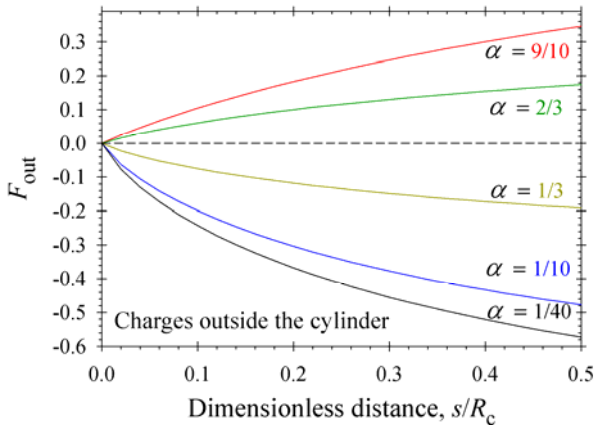


Fig. C2. Effect of cylinder radius R_c on the electrostatic interaction energy between the charge in the outer phase and the nonpolar phase inside the cylinder.

Fig. C2 summarizes numerical results for the effect of radius R_c on the electrostatic interaction energy for different ratios between dielectric constants. As should be, the general trends are quite similar to those in the case of sphere, see Fig. B2. The main difference is in the magnitude of the interaction energy – for cylinders at fixed distance s , the magnitudes are lower (about 2 times) than those for spheres.

In the case of dipoles in the outer dielectric phase, the electrostatic interaction difference, $u_d - u_d^0$, is given by Eq. (B33a), in which the exact expression for D_{out} reads:

$$D_{\text{out}} = \frac{2(1-2\alpha)s_1s_2(d^2 + 4s_1s_2)^{1/2}}{R_c[(s_1 + s_2)(d^2 + 4s_1s_2)^{1/2} - 4s_1s_2]} \left[C_{\text{out}}\left(\frac{s_1}{R_c}, \frac{s_1}{R_c}, 0, 0\right) + C_{\text{out}}\left(\frac{s_2}{R_c}, \frac{s_2}{R_c}, 0, 0\right) - 2C_{\text{out}}\left(\frac{s_1}{R_c}, \frac{s_2}{R_c}, \phi_d, z_d\right) \right] - (1-2\alpha) \quad (\text{C32})$$

see Eqs. (A6) and (C17). The dependencies of the calculated values of D_{out} on the system parameters are shown in Fig. 6 and discussed in the main text.

Charges and dipoles inside the dielectric cylinder. In this case the charge interaction energy is calculated from Eq. (C27). For large values of the parameter s/R_c , the asymptotic value of $C_{\text{inn}}(s/R_c, s/R_c, 0, 0)$ is equal to $R_c/(2s)$, as should be. Again for numerical calculations, it is convenient to exclude this singularity and to use the following equivalent representations of Eq. (C27):

$$\frac{u_c - u_c^0}{k_B T} = \frac{L_B z_c^2}{2s} F_{\text{inn}}, \quad F_{\text{inn}} \equiv (1-2\alpha) \left[\frac{2s}{R_c} C_{\text{inn}}\left(\frac{s}{R_c}, \frac{s}{R_c}, 0, 0\right) - 1 \right] \quad (\text{C33})$$

Fig. C3 summarizes numerical results for the effect of radius R_c on the interaction energy for different ratios between the dielectric constants. The general trends are quite similar to those in the case of sphere, see Fig. B4. The main difference is in the magnitude of the interaction energy – for cylinders at fixed distance s , the magnitudes are lower than those for spheres.

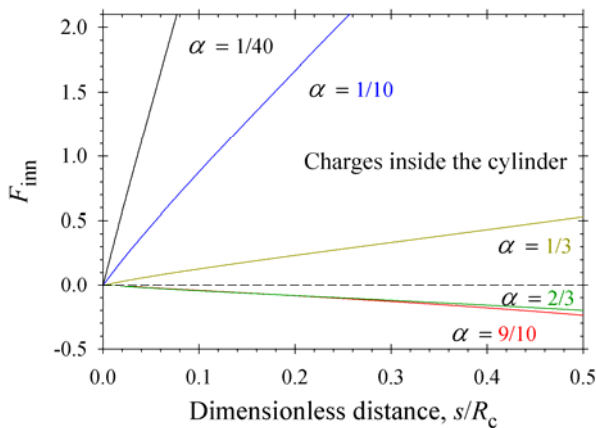


Fig. C3. Effect of cylinder radius R_c on the electrostatic interaction energy between the charge in the inner dielectric phase and the nonpolar phase outside the cylinder.

In the case of dipoles in the inner dielectric phase, the electrostatic interaction difference, $u_d - u_d^0$, is given by Eq. (B39a), in which the exact expression for D_{inn} reads:

$$D_{\text{inn}} = \frac{2(1-2\alpha)s_1s_2(d^2 + 4s_1s_2)^{1/2}}{R_c[(s_1 + s_2)(d^2 + 4s_1s_2)^{1/2} - 4s_1s_2]} [C_{\text{inn}}\left(\frac{s_1}{R_c}, \frac{s_1}{R_c}, 0, 0\right) + C_{\text{inn}}\left(\frac{s_2}{R_c}, \frac{s_2}{R_c}, 0, 0\right) - 2C_{\text{inn}}\left(\frac{s_1}{R_c}, \frac{s_2}{R_c}, \phi_d, z_d\right)] - (1-2\alpha) \quad (\text{C34})$$

see Eqs. (A6) and (C30). The dependencies of the calculated values of D_{inn} on the system parameters are shown in Fig. 7 and discussed in the main text.

Appendix D. Molecular aspects and parameters of the micellar model

In this section, we summarize all expressions and molecular parameters needed to calculate the sizes, shapes, and concentrations of micelles in the case of zwitterionic surfactants. The detailed explanation of the molecular thermodynamic model is published in Ref. [4].

D1. Molecular geometric parameters

Below all volumes, surface areas and radii refer to the micelle hydrocarbon core of alkyl chains with one end CH_3 group and $(n_c-1)\text{CH}_2$ groups, where n_c is the number of carbon atoms in the alkyl chain.

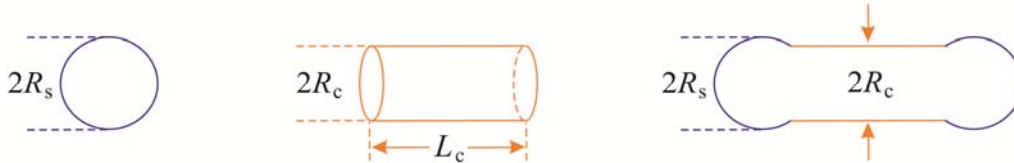


Fig. D1. Geometrical parameters of the hydrocarbon core of the spherical, the cylindrical part of spherocylindrical, and the spherocylindrical micelles.

Spherical micelles. The volume, V_s , the surface area, A_s , and the packing parameter, p , are related to the sphere radius, R_s , as follows:

$$V_s = \frac{4}{3}\pi R_s^3, \quad A_s = 4\pi R_s^2, \quad p = \frac{V_s}{A_s R_s} = \frac{1}{3} \quad (\text{D1})$$

see Fig. D1.

Cylindrical parts of spherocylindrical micelles. The cylinder volume, V_c , the lateral surface area, A_c , and the packing parameter, p , are simply related to the cylinder radius, R_c , and length, L_c , by the relationships:

$$V_c = \pi R_c^2 L_c, \quad A_c = 2\pi R_c L_c, \quad p = \frac{V_c}{A_c R_c} = \frac{1}{2} \quad (\text{D2})$$

see Fig. D1.

Spherical caps of spherocylindrical micelles. The endcaps have the shape of truncated spheres with sphere radius R_s and radius of the truncated circle of the cylindrical part, R_c (Fig. D1). The total volume of the two truncated spheres, V_{sc} , the total area of their spherical surfaces, A_{sc} , and the packing parameter, p , are calculated from the expressions:

$$V_{sc} = \frac{4}{3}\pi R_s^2 [R_s + (R_s^2 - R_c^2)^{1/2}] + \frac{2}{3}\pi R_c^2 (R_s^2 - R_c^2)^{1/2}, \quad R_c \leq R_s \quad (\text{D3})$$

$$A_{sc} = 4\pi R_s [R_s + (R_s^2 - R_c^2)^{1/2}], \quad R_c \leq R_s \quad (\text{D4})$$

$$p = \frac{V_{sc}}{A_{sc} R_s}, \quad \frac{1}{3} \leq p \leq \frac{3}{8} \quad (\text{D5})$$

Note that the minimal value of the packing parameter, $p = 1/3$, corresponds to hemispherical caps ($R_c = R_s$), whereas the maximal value, $p = 3/8$, is realized at $R_c / R_s = \sqrt{3}/2$.

The numbers of surfactant molecules contained in the cylindrical part, n_c , those in the spherical endcaps of a spherocylindrical micelle, n_s , and the total number of molecules, n_{tot} , are:

$$n_c = \frac{V_c}{v(n_c)}, \quad n_s = \frac{V_{sc}}{v(n_c)}, \quad n_{tot} = n_s + n_c \quad (\text{D6})$$

where $v(n_c)$ is the volume of the respective alkyl chain. We used the Tanford expressions for the extended chain length, l , and the chain volume, v :

$$l(n_c) = l(\text{CH}_3) + (n_c - 1)l(\text{CH}_2), \quad v(n_c) = v(\text{CH}_3) + (n_c - 1)v(\text{CH}_2) \quad (\text{D7})$$

For the length per CH_3 and CH_2 groups, the values $l(\text{CH}_3) = 2.8 \text{ \AA}$ and $l(\text{CH}_2) = 1.265 \text{ \AA}$ have been used. The volumes of the CH_3 and CH_2 groups, estimated from the absolute temperature, T , dependence of the volume of aliphatic hydrocarbons, are

$$v(\text{CH}_3) = [54.3 + 0.124(T - 298)] \text{ \AA}^3 \quad (\text{D8})$$

$$v(\text{CH}_2) = [26.9 + 0.0146(T - 298)] \text{ \AA}^3 \quad (\text{D9})$$

D2. Components of micelle free energy per molecule

For zwitterionic surfactant micelles, the standard free energy per molecule incorporated in an aggregate, f_k^0 , becomes a sum of five components [4]: f_σ – the contribution of the interfacial tension, σ , of the boundary between the micelle hydrocarbon core and the surrounding water phase at the micelle surface; f_{hs} – the steric repulsion between headgroups

of the surfactant molecules; f_{conf} – the conformational free energy of the surfactant hydrocarbon chains inside the micelle; f_{dip} – the new contribution from the zwitterionic dipole head and the hydrocarbon micellar core electrostatic interactions; μ_{m}^0 – the standard chemical potential of the surfactant molecule in the micelle. Here and hereafter, $R = R_{\text{c}}$ for the cylindrical part of a spherocylindrical micelle, $R = R_{\text{s}}$ for the spherical endcaps and spherical micelles, and p is the value of the packing parameter for the respective geometry.

Interfacial tension component. The interfacial free energy per molecule is calculated from the expression:

$$f_{\sigma} = \sigma(a - a_0), \quad a = \frac{v}{pR} \quad (\text{D10})$$

where a_0 is the surface area excluded by the surfactant head group and a is the area per surfactant molecule in the considered environment at the boundary between the micelle hydrocarbon core and the outer water phase.

The interfacial tension, σ , has been estimated using the generalized Tolman equation:

$$\sigma = \sigma_{\text{ow}} \left[1 + \frac{(1-p)\delta_{\text{T}}}{pR} \right]^{-1}, \quad \delta_{\text{T}} = 2.25 \frac{l(n_{\text{C}})}{l(11)} \text{ \AA} \quad (\text{D11})$$

where $\delta_{\text{T}}(n_{\text{C}})$ is the Tolman length and σ_{ow} is the interfacial tension between the bulk oil and water phases. The dependence of σ_{ow} on the absolute temperature, T , for different numbers of carbon atoms in the alkyl chains, n_{C} , is described by the following interpolation formula [4]:

$$\sigma_{\text{ow}} = [47.12 + 1.479n_{\text{C}}^{0.5422} - 0.0875(T - 293.15)] \text{ mN/m} \quad (\text{D12})$$

Headgroups steric repulsion component. The repulsion between surfactant headgroups at the micelle surface has been taken into account using the repulsion term in the two-dimensional equation of van der Waals:

$$\frac{f_{\text{hs}}}{k_{\text{B}}T} = -\ln\left(1 - \frac{a_0}{a}\right) \quad (\text{D13})$$

where a and a_0 have the same meanings as in Eq. (D10).

Chain-conformation component. This contribution to the micelle free energy describes the variety of conformations of surfactant hydrocarbon chains in the finite space of the micelle interior. The generalized version of the Semenov expression for the chain-conformation free energy per molecule [4]

$$\frac{f_{\text{conf}}}{k_{\text{B}}T} = \frac{3\pi^2 R^2}{4l_{\text{sg}}l} \frac{p^2}{1 + 3p + 2p^2} \quad (\text{D14})$$

was used with $l_{sg} = 4.6 \text{ \AA}$ and the concrete value of the extended length, $l(n_C)$, given by Eq. (D7).

Dipole-core interaction energy. These free energy components are described in Appendixes B and C. In the case of zwitterionic surfactant micelles, the dipoles are outside the micellar hydrocarbon core and the change of free energy component, f_{dip} , with respect to that for a planar interface, u_d^0 , is calculated from the obtained formula:

$$\frac{f_{dip}}{k_B T} = z_c^2 \left[\frac{L_B}{2s_1} + \frac{L_B}{2s_2} - \frac{2L_B}{(d^2 + 4s_1s_2)^{1/2}} \right] D_{out} \quad (D15)$$

see Eq. (B33a). The function D_{out} in the right-hand side of Eq. (D15) is calculated from Eqs. (B9) and (B33b) for the spherical endcaps and spherical micelles and respectively from Eq. (C13) and (C32) for cylindrical part of spherocylindrical micelles.

The dependence of the water dielectric constant, ε , on the absolute temperature, T , is given by the interpolation formula [5]:

$$\varepsilon = 87.74 - 0.40008(T - 273.15) + 9.398 \times 10^{-4}(T - 273.15)^2 - 1.41 \times 10^{-6}(T - 273.15)^3 \quad (D16)$$

The relative dielectric constants, ε_n , of dodecane and tetradecane at room temperature are 2.01 and 2.04, respectively [6].

Standard chemical potential. The standard chemical potential of the surfactant molecule in the micelle, μ_m^0 , accounts for molecular internal degrees of freedom and does not depend on the micelle shape and aggregation number. For simplification of the calculations, the value of u_d^0 , which is also independent on the micelle shape and the radii, is included in μ_m^0 .

D3. DDAO surface tension isotherm

To obtain the most probable surface area excluded by the surfactant headgroup, a_0 , we measured the dependence of the surface tension, σ , of dodecyldimethylamine oxide (DDAO) aqueous solutions (Fig. D2). The repulsion term in the two-dimensional equation of van der Waals is typically used to calculate the free energy component, f_{hs} , see Eq. (D13). Thus for the processing of experimental data in Fig. D2, the same type of the adsorption isotherm and the equation of state should be applied.

The van der Waals adsorption model for nonionic surfactants [7] consists of: i) the two-dimensional equation of state:

$$\sigma = \sigma_0 - k_B T \frac{\Gamma}{1 - a_0 \Gamma} + \beta \Gamma^2 \quad (D17)$$

where Γ is the adsorption, σ_0 is the surface tension of the pure solvent, and β is a parameter, accounting for the interaction between the adsorbed molecules; ii) the adsorption isotherm:

$$Kc = \frac{a_0\Gamma}{1-a_0\Gamma} \exp\left(\frac{a_0\Gamma}{1-a_0\Gamma} - \frac{2\beta}{k_B T}\Gamma\right) \quad (\text{D18})$$

relates the surfactant concentration, c (mM), and the adsorption constant, K , with the adsorption, Γ . The solid lines in Fig. D2 show the obtained best theoretical fit with the van der Waals adsorption model, Eqs. (D17) and (D18). The obtained parameters are: $a_0 = 35 \text{ \AA}^2$; $K = 175 \text{ (mM)}^{-1}$; $\beta/(a_0 k_B T) = 1.49$. The theoretical calculations show that the adsorption increases with the rise of DDAO concentration and the value of the saturation adsorption (at the CMC) is $3.97 \text{ } \mu\text{mol/m}^2$.

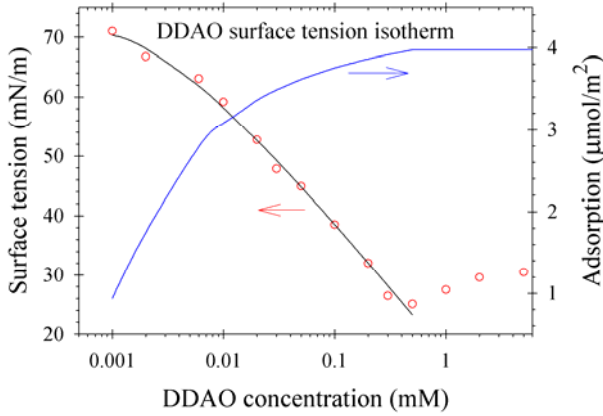


Fig. D2. Surface tension isotherm of DDAO aqueous solutions and the theoretical fit with van der Waals model, i.e. Eqs. (D17) and (D18). The determined surface adsorption is plotted on the right axis.

D4. Free energy components and the CMC determination

Fig. D3a shows the dependence of the free energy components and Δf_c on the radius of the micelle cylindrical part, R_c , for TDAO micelles. The increase of the radius R_c leads to the decrease of f_σ , and the increase of f_{hs} , f_{conf} , and f_{dip} . The minimum of $\Delta f_c = 4.45 k_B T$ is achieved for the optimal radius of the cylindrical part $R_c = 15.33 \text{ \AA}$. The dependence of the excess free energy components for TDAO micelles on the radius of the spherical endcaps is shown in Fig. D3b. The total aggregation number of the spherical endcaps, n_s , increases with the cube of radius R_s . The non-shielded area of hydrocarbon/water contact decreases with the decrease of surface curvature and as a result $(E_{sc})_\sigma$ decreases with the rise of R_s . In contrast, both $(E_{sc})_{hs}$ and $(E_{sc})_{conf}$ are increasing functions of R_s . Note that $|f_{dip}|$ decreases with the rise of radii of cylindrical part and spherical endcaps of micelles (see Sections 2 and 3). Nevertheless, $|(E_{sc})_{dip}|$ increases with the rise of R_s , because of the faster increase of n_s .

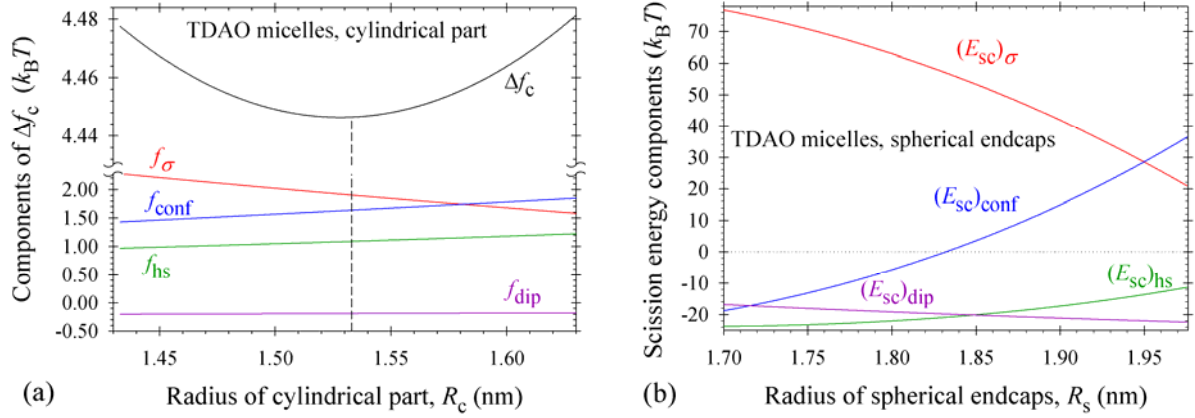


Fig. D3. Plots of: (a) Δf_c vs. R_c for the micelle cylindrical part; (b) scission energy components vs. R_s for the micelle spherical endcaps for TDAO. The vertical dashed line corresponds to the position of the Δf_c minimum.

The critical micelle concentration has been estimated as that value of the monomer concentration, X_1 , for which the concentration of singly dispersed surfactant molecules is equal to that of surfactant present in the form of aggregates. All molecular parameters and optimal shapes of micellar aggregates are defined – the only free parameter is the standard chemical potential difference.

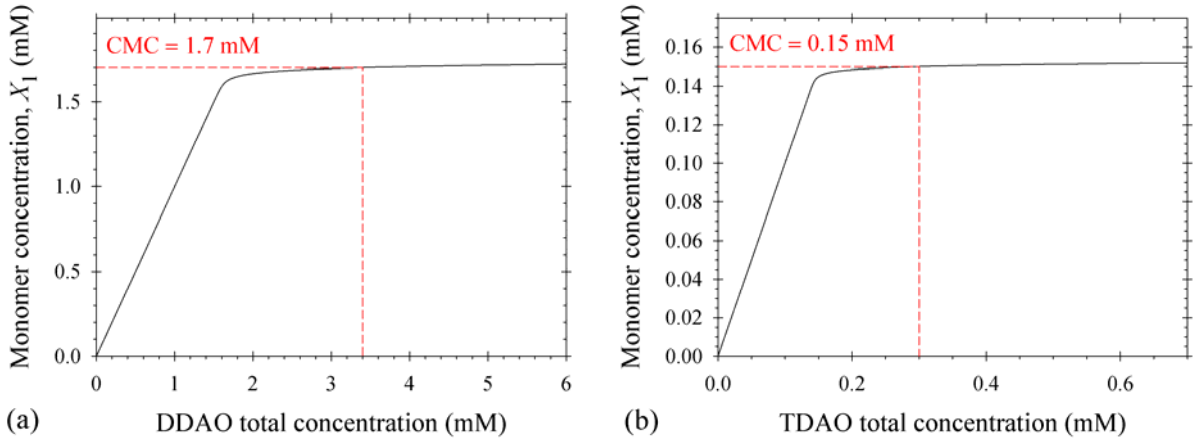


Fig. D4. Dependence of the monomer concentration, X_1 , on the total surfactant concentration: (a) DDAO micellar solutions; (b) TDAO micellar solutions.

Fig. D4 shows the dependence of X_1 on the total surfactant concentration, X_s . At the experimental CMC value (1.7 mM for DDAO and 0.15 mM for TDAO), the total surfactant concentration, X_s , is equal to $2X_1$ (3.4 mM for DDAO and 0.30 mM for TDAO). As a result, we calculated that $\mu_1^0 - \mu_m^0$ is equal to $14.49 k_B T$ for DDAO and to $17.21 k_B T$ for TDAO.

References

- [1] L.D. Landau, E.M. Lifshitz, L.P. Pitaevskii, *Electrodynamics of Continuous Media*, Elsevier Butterworth-Heinemann, Oxford, 2004.
- [2] D.V. Redžić, M.S.A. Eldakli, M.D. Redžić, Image charge inclusion in the dielectric sphere revisited, *Eur. J. Phys.* 33(6) (2012) 1751–1759,
<https://doi.org/10.1088/0143-0807/33/6/1751>.
- [3] S.T. Cui, Electrostatic potential in cylindrical dielectric media using the image charge method, *Mol. Phys.* 104(19) (2006) 2993–3001,
<http://dx.doi.org/10.1080/00268970600926647>.
- [4] K.D. Danov, P.A. Kralchevsky, S.D. Stoyanov, J.L. Cook, I.P. Stott, E.G. Pelan, Growth of wormlike micelles in nonionic surfactant solutions: Quantitative theory vs. experiment, *Adv. Colloid Interface Sci.* 256 (2018) 1–22,
<https://doi.org/10.1016/j.cis.2018.05.006>.
- [5] K.D. Danov, P.A. Kralchevsky, R.D. Stanimirova, S.D. Stoyanov, J.L. Cook, I.P. Stott, Analytical modeling of micellar growth. 4. Molecular thermodynamics of wormlike micelles from ionic surfactants: Theory vs. experiment, *J. Colloid Interface Sci.* 584 (2021) 561–581,
<https://doi.org/10.1016/j.jcis.2020.10.004>.
- [6] C. Wohlfarth, *Static Dielectric Constants of Pure Liquids and Binary Liquid Mixtures*, Supplement to Vol. IV/17, M.D. Lechner (Ed.), Landolt-Börnstein: Numerical Data and Functional Relationships in Science and Technology, Springer, 2015.
- [7] K.D. Danov, P.A. Kralchevsky, K.P. Ananthapadmanabhan, A. Lips, Interpretation of surface–tension isotherms of *n*-alkanoic (fatty) acids by means of the van der Waals model, *J. Colloid Interf. Sci.* 300 (2006) 809–813,
<http://dx.doi.org/10.1016/j.jcis.2006.04.026>.